

## SPECTRAL CLASSIFICATION AND REDSHIFT MEASUREMENT FOR THE SDSS-III BARYON OSCILLATION SPECTROSCOPIC SURVEY

ADAM S. BOLTON<sup>1</sup>, DAVID J. SCHLEGEL<sup>2</sup>, ÉRIC AUBOURG<sup>3,4</sup>, STEPHEN BAILEY<sup>2</sup>, VAISHALI BHARDWAJ<sup>5</sup>,  
JOEL R. BROWNSTEIN<sup>1</sup>, SCOTT BURLES<sup>6</sup>, YAN-MEI CHEN<sup>7</sup>, KYLE DAWSON<sup>1</sup>, DANIEL J. EISENSTEIN<sup>8</sup>, JAMES E. GUNN<sup>9</sup>,  
G. R. KNAPP<sup>9</sup>, CRAIG P. LOOMIS<sup>9</sup>, ROBERT H. LUPTON<sup>9</sup>, CLAUDIA MARASTON<sup>10</sup>, DEMITRI MUNA<sup>11</sup>, ADAM D. MYERS<sup>12</sup>,  
MATTHEW D. OLMSTEAD<sup>1</sup>, NIKHIL PADMANABHAN<sup>13</sup>, ISABELLE PÂRIS<sup>14,15</sup>, WILL J. PERCIVAL<sup>10</sup>, PATRICK PETITJEAN<sup>14</sup>,  
CONSTANCE M. ROCKOSI<sup>16</sup>, NICHOLAS P. ROSS<sup>2</sup>, DONALD P. SCHNEIDER<sup>17,18</sup>, YIPING SHU<sup>1</sup>, MICHAEL A. STRAUSS<sup>9</sup>,  
DANIEL THOMAS<sup>10</sup>, CHRISTY A. TREMONTI<sup>7</sup>, DAVID A. WAKE<sup>19</sup>, BENJAMIN A. WEAVER<sup>11</sup>, AND  
W. MICHAEL WOOD-VASEY<sup>20</sup>

*Draft version September 12, 2012*

### ABSTRACT

We describe the automated spectral classification, redshift determination, and parameter measurement pipeline in use for the Baryon Oscillation Spectroscopic Survey (BOSS) of the Sloan Digital Sky Survey III (SDSS-III) as of the survey’s Ninth Data Release (DR9), encompassing 831,000 moderate-resolution optical spectra. We give a review of the algorithms employed, and describe the changes to the pipeline that have been implemented for BOSS relative to previous SDSS-I/II versions, including new sets of stellar, galaxy, and quasar redshift templates. For the color-selected “CMASS” sample of massive galaxies at redshift  $0.4 \lesssim z \lesssim 0.8$  targeted by BOSS for the purposes of large-scale cosmological measurements, the pipeline achieves an automated classification success rate of 98.7% and confirms 95.4% of unique CMASS targets as galaxies (with the balance being mostly M stars). Based on visual inspections of a subset of BOSS galaxies, we find that approximately 0.2% of confidently reported CMASS sample classifications and redshifts are incorrect, and about 0.4% of all CMASS spectra are objects unclassified by the current algorithm which are potentially recoverable. The BOSS pipeline confirms that  $\sim 51.5\%$  of the quasar targets have quasar spectra, with the balance mainly consisting of stars and low signal-to-noise spectra. Statistical (as opposed to systematic) redshift errors propagated from photon noise are typically a few tens of  $\text{km s}^{-1}$  for both galaxies and quasars, with a significant tail to a few hundreds of  $\text{km s}^{-1}$  for quasars. We test the accuracy of these statistical redshift error estimates using repeat observations, finding them underestimated by a factor of 1.19 to 1.34 for galaxies, and by a factor of 2 for quasars. We assess the impact of sky-subtraction quality, signal-to-noise ratio, and other factors on galaxy redshift success. Finally, we document known issues with the BOSS DR9 spectroscopic data set, and describe directions of ongoing development.

*Subject headings:* methods: data analysis—techniques: spectroscopic—surveys

<sup>1</sup> Department of Physics and Astronomy, University of Utah, 115 South 1400 East, Salt Lake City, UT 84112, USA (bolton@astro.utah.edu)

<sup>2</sup> Lawrence Berkeley National Laboratory, 1 Cyclotron Rd., Berkeley, CA 94720, USA

<sup>3</sup> Astroparticule et Cosmologie (APC), Université Paris-Diderot, 75205 Paris Cedex 13, France

<sup>4</sup> CEA, Centre de Saclay, Irfu/SPP, F-91191 Gif-sur-Yvette, France

<sup>5</sup> Department of Astronomy, University of Washington, 3910 15th Ave. NE, Seattle, WA 98195, USA

<sup>6</sup> Cutler Group, LP, 101 Montgomery St., Suite 700, San Francisco, CA 94104, USA

<sup>7</sup> Department of Astronomy, University of Wisconsin, 475 North Charter St., Madison, WI 53706, USA

<sup>8</sup> Harvard-Smithsonian Center for Astrophysics, 60 Garden St., Cambridge, MA 02138, USA

<sup>9</sup> Department of Astrophysical Sciences, Peyton Hall, Princeton University, 4 Ivy Ln., Princeton, NJ 08544, USA

<sup>10</sup> Institute of Cosmology and Gravitation, University of Portsmouth, Portsmouth PO1 3FX

<sup>11</sup> Center for Cosmology and Particle Physics, New York University, 4 Washington Pl., New York, NY 10003, USA

<sup>12</sup> Department of Physics and Astronomy, University of Wyoming, Laramie, WY 82071, USA

<sup>13</sup> Department of Physics, Yale University, 260 Whitney Ave., New Haven, CT 06520, USA

<sup>14</sup> Institut d’Astrophysique de Paris, UPMC-CNRS, UMR7095, 98bis Blvd. Arago, 75014 Paris, France

<sup>15</sup> Departamento de Astronomía, Universidad de Chile, Casilla

### 1. INTRODUCTION

The Sloan Digital Sky Survey III (SDSS-III, Eisenstein et al. 2011) is the third phase of the SDSS (York et al. 2000).<sup>21</sup> Within the SDSS-III, the Baryon Oscillation Spectroscopic Survey (BOSS, Dawson et al. 2012) is currently mapping a larger volume of the universe than any previous spectroscopic survey. The Ninth Data Release of the SDSS-III (DR9, Ahn et al. 2012, released publicly on 2012 July 31) is the first SDSS-III data release to include BOSS spectroscopic data, and comprises good observations of 831 unique plate-pluggings

36-D, Santiago, Chile

<sup>16</sup> UCO/Lick Observatory, University of California, Santa Cruz, 1156 High St., Santa Cruz, CA 95064, USA

<sup>17</sup> Department of Astronomy and Astrophysics, The Pennsylvania State University, University Park, PA 16802, USA

<sup>18</sup> Institute for Gravitation and the Cosmos, The Pennsylvania State University, University Park, PA 16802, USA

<sup>19</sup> Department of Astronomy, Yale University, 260 Whitney Ave., New Haven, CT 06520, USA

<sup>20</sup> Department of Physics and Astronomy, University of Pittsburgh, 100 Allen Hall, 3941 O’Hara St., Pittsburgh, PA 15260, USA

<sup>21</sup> Throughout this paper, we will refer to the earlier SDSS phases collectively as SDSS-I/II.

of 813 unique tilings (plates worth of targets) on the sky. Each plate delivers simultaneous spectroscopic observations of 1000 lines of sight with optical fibers that feed a pair of two-arm spectrographs, giving a total of 831,000 BOSS DR9 spectra.

The main science goal of BOSS is to trace the large-scale mass structure of the universe using massive galaxies and quasar Ly $\alpha$  absorption systems, in order to measure the length scale of the “baryon acoustic oscillation” feature in the spatial correlation function of these objects (e.g., Eisenstein et al. 2005), and thereby to constrain the nature of the dark energy that drives the accelerated expansion of the present-day universe. To meet this goal, the BOSS project has specified a series of scientific requirements, including: (1) an RMS galaxy redshift precision better than 300 km s $^{-1}$ ; (2) a galaxy redshift success rate of at least 94%, including both targeting inefficiency and spectroscopic redshift failure; (3) a catastrophic galaxy redshift error rate of less than 1%; and (4) spectroscopic confirmation of at least 15 quasars at  $2.2 < z < 3.5$  per degree $^2$  from among no more than 40 targets per degree $^2$ . To satisfy these requirements within such a large survey, automated spectroscopic calibration, extraction, classification, and redshift measurement methods are essential.

This paper, one of a series of technical papers describing SDSS-III DR9 in general and the BOSS data set in particular, presents the automated classification and redshift measurement software for the main galaxy and quasar target samples implemented for the BOSS project. This software is written in the IDL language, and is titled `idlspec2d`. Earlier versions of this code were used to analyze SDSS-I/II data (see Aihara et al. 2011), alongside the complementary and independently developed pipeline software `spectroid` (see SubbaRao et al. 2002 and Adelman-McCarthy et al. 2006); for the BOSS project, the `idlspec2d` software has been adopted as the primary code, due to its robust error estimation methods and its tight integration of redshift measurement and classification with the lower-level operations of raw data calibration and extraction. The code has also been upgraded with new redshift-measurement templates and several new algorithms in order to meet the scientific requirements of the BOSS project. The tagged software version `v5.4.45` was used to process all BOSS spectroscopic data for DR9 $^{22}$ , and the classification and redshift results delivered by this code have been used for recently published BOSS DR9-sample cosmological analyses (Anderson et al. 2012; Manera et al. 2012; Nuza et al. 2012; Reid et al. 2012; Ross et al. 2012a; Sanchez et al. 2012; Tojeiro et al. 2012). An overview of the BOSS project, including experimental design, scientific goals, observational operations, and ancillary programs, is given in Dawson et al. (2012). A description of the `idlspec2d` calibration and extraction methods which transform raw CCD pixel data into one-dimensional object spectra will be presented in Schlegel et al. (2012).

The organization of this paper is as follows. Section 2 presents an overview of the spectroscopic data sample of BOSS DR9. Section 3 describes the classification and redshift pipeline algorithms and procedures, including

the core redshifting algorithm (§3.1), special classification handling for the galaxy target samples (§3.2), measured spectroscopic parameters (§3.3), and output files (§3.4). Section 4 describes the templates constructed for the automated spectroscopic identification and redshift analysis of BOSS galaxies (§4.1), quasars (§4.2), and stars (§4.3). Section 5 analyzes the completeness, purity, accuracy, and precision of the samples classified and measured by the `idlspec2d` pipeline. Section 6 documents known issues in the DR9 release of BOSS data, and §7 provides a summary and conclusions.

## 2. DATA OVERVIEW

The main BOSS survey program consists of two galaxy target samples (Padmanabhan et al. 2012) and a quasar target sample including both color-selected candidates and known quasars (Bovy et al. 2011; Kirkpatrick et al. 2011; Ross et al. 2012b). The galaxy samples are designated CMASS (for “constant mass”) and LOWZ (for “low-redshift”). The LOWZ galaxy sample is composed of massive red galaxies spanning the redshift range  $0.15 \lesssim z \lesssim 0.4$ . The CMASS galaxy sample is composed of massive galaxies spanning the redshift range  $0.4 \lesssim z \lesssim 0.7$ . Both samples are color-selected to provide near-uniform sampling over the combined volume. The faintest galaxies are at  $r = 19.5$  for LOWZ and  $i = 19.9$  for CMASS. Colors and magnitudes for the galaxy selection cuts are corrected for Galactic extinction using Schlegel et al. (1998) dust maps. The BOSS quasar sample is selected to recover as many objects as possible in the redshift range  $2.2 < z < 3.5$  for the purposes of measuring the 3D structure in the Ly $\alpha$  forest. A variety of selection algorithms are employed to select the quasar sample, which lies close to the color locus of F stars. The faint-end magnitude limits of the quasar target sample are extinction-corrected PSF magnitudes of  $g = 22$  and  $r = 21.85$ .

A summary of the DR9 BOSS spectroscopic data set (observed between 2009 December and 2011 July) is given in Table 1, along with performance metrics that will be discussed in detail further below. Representative BOSS survey spectra are shown in Figure 1. The automated classification and measurement software described here is applied to all spectra obtained by the BOSS spectrographs (Smee et al. 2012), including spectra targeted under ancillary programs described in Dawson et al. (2012). In this work we focus on the analysis of the main BOSS galaxy and quasar survey targets, since the performance on these samples is the primary scientific driver of the design, development, and verification of the pipeline.

For the purposes of this paper, we define the samples of unique LOWZ and CMASS spectra according to the following cuts:

1. Selected by the appropriate sample color cuts (encoded by bit 0 of the `BOSS_TARGET1` mask for the LOWZ sample, and by bit 1 of that mask for the CMASS sample.) The LOWZ and CMASS samples are not mutually exclusive, although they are mostly non-overlapping.
2. Observed with a spectroscopic fiber that is well plugged, successfully mapped to the target object,

<sup>22</sup> The DR9 tagged version of `idlspec2d` can be obtained at [www.sdss3.org/svn/repo/idlspec2d/tags/v5.4.45/](http://www.sdss3.org/svn/repo/idlspec2d/tags/v5.4.45/).

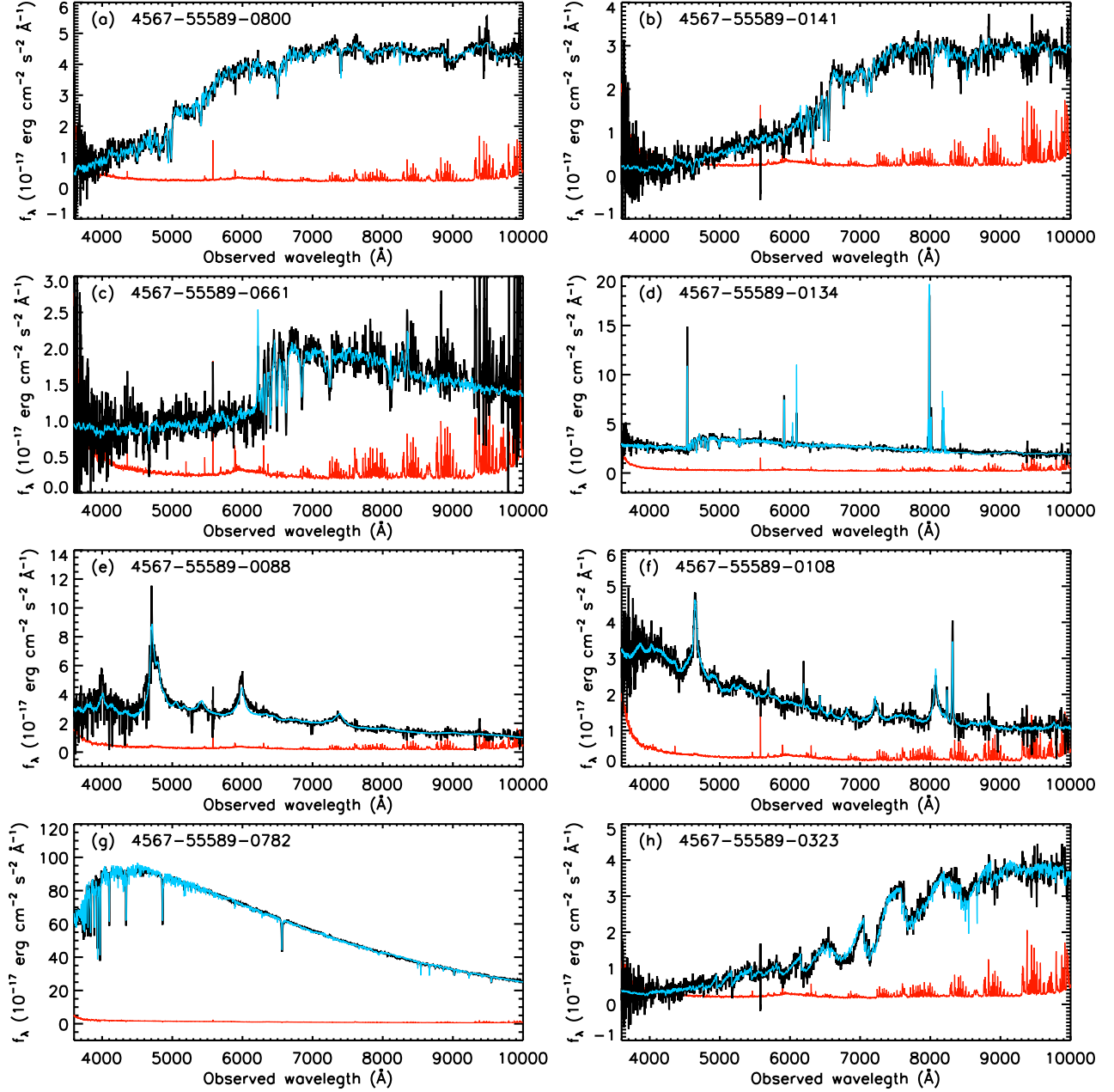


FIG. 1.— Mosaic of representative BOSS spectra, with a resolution of  $R \approx 2000$ . Black lines show data (smoothed over a 5-pixel window), cyan lines show best-fit redshift/classification model, and red lines show  $1\text{-}\sigma$  noise level estimated by the extraction pipeline. Spectra are labeled by PLATE-MJD-FIBERID. Individual objects are: (a) redshift  $z = 0.256$  LOWZ galaxy; (b) redshift  $z = 0.649$  CMASS galaxy; (c) redshift  $z = 0.669$  CMASS galaxy with post-starburst continuum; (d) redshift  $z = 0.217$  starburst galaxy (from QSO target sample); (e) redshift  $z = 2.873$  quasar; (f) redshift  $z = 0.661$  quasar; (g) spectrophotometric standard star; (h) M star (from CMASS target sample).

and not affected by bad CCD columns that remove a large fraction of the wavelength coverage. These conditions are reported via bits 1 and 7 of the ZWARNING bitmask described in §3.1.

3. Apparent (not extinction-corrected)  $i$ -band magnitude less than 21.5 within a  $2''$ -diameter circular aperture, corresponding to the angular size of the BOSS fibers. This criterion excludes low surface-brightness targets for which the spectroscopic signal-to-noise ratio (S/N) becomes unacceptably low for nominal survey exposure times of 60 minutes in good conditions.

4. Best single observation within the survey data set, for the case of multiply observed spectra. This designation is described in §3.4.

The sample of unique BOSS quasar spectra for the current work is defined according to the following cuts:

1. Selected from one of the four categories of known quasars with redshifts optimal for Ly $\alpha$  forest analysis (bit 12 of the BOSS\_TARGET1 mask), quasars selected from the FIRST survey (bit 18, Becker et al. 1995), and candidates from the BOSS “Core” and “Bonus” quasar candidate selection algorithms (bits 40 and 41 respectively: see Ross et al. 2012b).

TABLE 1  
BOSS DR9 SUMMARY SPECTRUM TOTALS

Item	Number
Plate pluggings	831
Unique plates	819
Unique tiles (plates worth of targets)	813
Spectra	831000
Effective spectra <sup>1</sup>	829073
Unique spectra	763425
CMASS sample spectra	353691
Unique CMASS spectra	324198
Unique CMASS with ZWARNING_NOQSO == 0 <sup>2</sup>	320031
Unique CMASS that are galaxies	309307
LOWZ sample spectra	111347
Unique LOWZ spectra	103729
Unique LOWZ with ZWARNING_NOQSO == 0 <sup>2</sup>	103610
Unique LOWZ that are galaxies	102890
CMASS && LOWZ sample spectra	3201
Unique CMASS && LOWZ spectra	2990
Unique CMASS && LOWZ with ZWARNING_NOQSO == 0 <sup>2</sup>	2976
Unique CMASS && LOWZ that are galaxies	2935
Quasar sample spectra <sup>3</sup>	166034
Unique quasar sample spectra	154433
Unique quasar sample with ZWARNING == 0 <sup>4</sup>	122488
Unique quasar sample spectra that are quasars	79570
Number of above with $2.2 \leq z \leq 3.5$	51903
Unique quasar sample scanned visually	154173
Visual $2.2 \leq z \leq 3.5$ quasars missed by pipeline	895
Pipeline $2.2 \leq z \leq 3.5$ QSOs with visual disagreement <sup>5</sup>	327
Sky spectra	78573
Unique sky-spectrum lines of sight	75850
Spectrophotometric standard star spectra	16905
Unique standard star spectra	14915
Ancillary program spectra	32381
Unique ancillary target spectra	28968
Other spectra (commissioning, calibration, etc.)	74620
Unique other spectra	65461

<sup>a</sup>Excludes unplugged fibers and spectra falling on bad CCD columns.

<sup>b</sup>ZWARNING\_NOQSO == 0 indicates a confident spectroscopic classification and redshift measurement for galaxy targets (see §3.1 and §3.2).

<sup>c</sup>“Quasar targets” tabulated here are from the main survey quasar sample, and exclude any ancillary and calibration quasar targets.

<sup>d</sup>ZWARNING == 0 indicates a confident spectroscopic classification and redshift measurement for quasar targets (see §3.1).

<sup>e</sup>“Visual disagreement” is either  $|\Delta z| > 0.05$  between pipeline and visual inspections, or absence of confident visual classification & redshift.

2. Plugged, mapped, and well-covered in wavelength (as for Item 2 of the previous list for galaxy targets).
3. Best single observation within the survey data set (as for Item 4 of the previous list).

### 3. PIPELINE OVERVIEW

Imaging and spectroscopic data for the BOSS Survey are obtained with the 2.5-m Sloan Telescope at Apache Point Observatory (Gunn et al. 2006), first with the imaging camera (Gunn et al. 1998) and then with an upgraded (relative to SDSS-I/II) spectrograph system capable of obtaining 1000 spectra simultaneously using optical fibers plugged into a drilled aluminum focal plate and feeding two double-arm spectrographs. The characteristics of this instrument are summarized in Table 2,

TABLE 2  
BOSS SPECTROGRAPH SYSTEM CHARACTERISTICS

Parameter	Value
On-sky field of view	3° diameter
Fiber aperture	2" diameter
Multiplex capability	1,000 objects
Wavelength coverage	$3,600 \text{ \AA} \lesssim \lambda \lesssim 10,400 \text{ \AA}$
Spectral resolution	$\lambda/\Delta\lambda \approx 2,000$

and described in detail by Smee et al. (2012). The outputs of the fibers feeding each spectrograph are arrayed linearly along a “slit-head” and numbered within the spectroscopic pipeline by the sequential index FIBERID, which by convention runs from 1–500 in spectrograph 1 and from 501–1000 in spectrograph 2. A unique physical target plate is specified by the PLATE identifier. Since the same plate can be plugged and observed on multiple occasions, with different mappings between fibers and target holes, the modified Julian date of a unique plugging is tracked as well via the MJD parameter. Together, the combination of PLATE, MJD, and FIBERID constitute a unique identifier for a BOSS spectrum (as was also the case for SDSS-I/II spectra). Each plugging is observed with multiple exposures which are exactly 15 minutes each in length and can be distributed across more than one night of observation. Typically four to six exposures are required to attain sufficient S/N per pixel at a fiducial magnitude. All good data from a unique plugging are co-added together during the spectroscopic data reduction process. Data from different pluggings are never combined together.

The wavelength calibration, extraction, sky subtraction, flux calibration, and co-addition of BOSS spectra from raw CCD pixel data are described in Schlegel et al. (2012). The extraction implementation is a variation of the optimal-extraction algorithm described by Hewett et al. (1985) and Horne (1986), including a forward-modeling solution that de-blends the cross-talk between neighboring fibers on the CCD. (A similar approach is described in Sandin et al. 2010.) The outputs of this “two-dimensional” pipeline software are stored on a plate-by-plate basis for sets of 1000 spectra in the multi-extension “spPlate” FITS files, which are the inputs to the “one-dimensional” (1D) pipeline software described in this work. The full contents of the spPlate files are described in detail in the online data model<sup>23</sup>; for the purposes of the redshift measurement and classification pipeline, the most important products are:

1. Wavelength-calibrated, sky-subtracted, flux-calibrated, and co-added object spectra, rebinned onto a uniform baseline of  $\Delta \log_{10} \lambda = 10^{-4}$  (about  $69 \text{ km s}^{-1}$ ) per pixel.
2. Statistical error-estimate vectors for each spectrum (expressed as inverse variance) incorporating contributions from photon noise, CCD read noise, and sky-subtraction error.
3. Mask vectors for each spectrum identifying pixels where warning conditions exist in either any

<sup>23</sup> <http://www.sdss3.org/dr9/>

(ORMASK) or all (ANDMASK) of the spectra contributing to the final co-added spectrum.

### 3.1. Redshift measurement and classification

The BOSS spectral classification and redshift-finding analysis is approached as a  $\chi^2$  minimization problem. Linear fits are made to each observed spectrum using multiple templates and combinations of templates evaluated for all allowed redshifts, and the global minimum- $\chi^2$  solution is adopted for the output classification and redshift. This approach requires the spectra and their errors to be well-understood, and requires the template spectra to sufficiently span the observed space. Both these conditions are satisfied for the BOSS galaxy and quasar targets, resulting in accurate redshift fits and enabling a quantitative assessment of the confidence of those fits. By performing a statistically objective analysis, confident redshifts are obtained even for data at lower S/N where manual inspection may fail.

The basic outputs of the redshift determination and classification algorithm described in this section are the measured redshift  $Z$ , its associated 1-sigma statistical error  $Z\_ERR$ , a classification category  $CLASS$  (either "GALAXY", "QSO" for quasar, or "STAR"), and a confidence flag  $ZWARNING$  that is zero for confident measurements and non-zero otherwise. Section 3.2 describes special variations on these outputs that are recommended for use with the BOSS LOWZ and CMASS galaxy sample spectra.

The least-squares minimization is performed by comparison of each spectrum to a full range of templates spanning galaxies, quasars, and stars. A range of redshifts is explored, with trial redshifts spaced every pixel ( $69 \text{ km s}^{-1}$ ) for most templates and spaced by four pixels ( $276 \text{ km s}^{-1}$ ) for quasar templates. At each redshift the spectrum is fit with an error-weighted least-squares linear combination of redshifted template "eigenspectra" in combination with a low-order polynomial. The polynomial terms absorb Galactic extinction, intrinsic extinction, and residual spectro-photometric calibration errors (typically at the 10% level) that are not fully spanned by the eigenspectra. The template basis sets are derived from rest-frame principal-component analyses (PCA) of training samples of galaxies, quasars, and cataclysmic variable stars, and from a set of archetype spectra for other types of stars. CV stars are handled as a separate class from other stars due to their significant range of emission-line strengths. The construction of these basis sets is described in detail in §4 below. This best-fit combination model gives a  $\chi^2$  value for that trial redshift, and these values define a  $\chi^2(z)$  curve when computed across the redshift range under consideration. To facilitate comparison between template classes with differing numbers of basis vectors, these  $\chi^2$  values are analyzed in reduced form  $\chi_r^2$ , i.e., divided by the number of degrees of freedom. In practice this is nearly equivalent to working in terms of  $\chi^2$  for any given spectrum, as the number of pixels ( $\sim 4500$ ) greatly exceeds the number of free parameters in all fits. The best redshifts for a particular class under consideration are defined by the locations of the lowest minima in the  $\chi_r^2$  curve, where that curve is fit by a quadratic function using the five points nearest the minimum (11 points for quasars). The initial quasar fits where the trial redshifts are spaced every four pixels

are re-fit near the five best fits with redshifts spaced every pixel. This two-step fitting for the quasars is done for computational efficiency, since most of the computational time is spent evaluating quasar fits which are performed on all targets. The statistical error on the final redshift is evaluated at the location of the minimum of the  $\chi^2$  curve as the change in redshift  $\pm \delta z$  for which  $\chi^2$  increases by one above the minimum value. Noise in the spectra can result in multiple local minima in the neighborhood of the global minimum that are not significant. These are typically separated by a few pixels, or  $\sim 200 \text{ km s}^{-1}$ . For all template fits, we collapse minima separated by less than  $1000 \text{ km s}^{-1}$  to a single minimum. Solutions with separations exceeding  $1000 \text{ km s}^{-1}$  must be explicitly evaluated since they represent catastrophic redshift failures for BOSS galaxies if they are statistically indistinguishable from one another (see panel "h" of Figure 15 further below). The redshift-finding procedure is shown schematically in Figure 2. (See also Glazebrook et al. 1998.)

This core algorithm is applied within the pipeline according to the following sequence:

1. Read the spectrum, error estimates, and mask vectors for a single spectroscopic plate from the `spPlate` file.
2. Mask pixels outside the range  $3600 \text{ \AA} - 10400 \text{ \AA}$ , pixels at wavelengths where the typical sky-subtraction model residuals are more than 3-sigma worse than the errors expected from a Poisson model in any sub-exposure (BADSKYCHI set in the ORMASK vector output by the reduction software; Schlegel et al. 2012), pixels where the sky brightness is in excess of the extracted object flux plus ten times its statistical error in all sub-exposures (BRIGHTSKY set in the ANDMASK), and pixels with negative flux at greater than  $10\text{-}\sigma$  significance.
3. Find the best five galaxy redshifts between  $z = -0.01$  and  $z = 1.0$ , using a rest-frame template basis of four eigenspectra (§4.1).
4. Find the best five quasar redshifts between  $z = 0.0033$  and  $z = 7.0$ , using a rest-frame template basis of four eigenspectra (§4.2).
5. Find the best single redshift for each of 123 subclasses of star from  $-1200 \text{ km s}^{-1}$  to  $+1200 \text{ km s}^{-1}$ , using a single rest-frame archetype spectrum for each one (§4.3).
6. Find the best single cataclysmic variable star redshift from  $-1000 \text{ km s}^{-1}$  to  $+1000 \text{ km s}^{-1}$ , using a rest-frame template basis of three eigenspectra (in order to capture emission-line strength variations, §4.3.)
7. Sort all redshifts and classifications together by ascending  $\chi_r^2$ , and assign the best spectroscopic redshift and classification from among GALAXY, QSO (quasar), and STAR (including CV) based on the overall minimum  $\chi_r^2$  across all classes and redshifts.

8. Compare the change in  $\chi_r^2$  between the best classification and redshift and the next-best classification and redshift with a velocity difference greater than  $1000 \text{ km/s}^{-1}$ , and assign a low-confidence “ZWARNING” flag if this difference is either less than 0.01 in absolute terms or less than 0.01 times the overall minimum  $\chi_r^2$  value. For the  $\sim 4500$  degrees of freedom typical of a BOSS spectrum, the absolute threshold of  $\Delta\chi_r^2 = 0.01$  corresponds to  $\Delta\chi^2 \approx 45$  (naively interpreted as 6.7-sigma). The relative requirement on  $\Delta\chi_r^2$  serves to make the statistical confidence threshold progressively more conservative at higher S/N levels where the redshift templates fits are worse in an absolute sense but nevertheless have greater distinguishing power among multiple hypotheses.

The threshold value of  $\Delta\chi_r^2 > 0.01$  used to assign confidence to the classifications is empirically determined. The threshold could be lowered further to recover more redshifts but at the cost of more mis-classifications and incorrect redshifts. Tests on repeat CMASS sample data show that decreasing the threshold to 0.008 (0.005) would increase redshift completeness by 0.3% (0.6%), with 8% (16%) of the added measurements being incorrect. (A full analysis of BOSS galaxy redshift completeness and purity is given in §5.1.) An additional test is made possible by the nearly 80,000 blank BOSS sky spectra in DR9. Among these, 2% fit a template with a confidence  $\Delta\chi_r^2 > 0.01$ , implying they would be assigned a confident redshift in the absence of prior knowledge of their status as blank sky spectra. (Although a small fraction of these are in fact real objects detected spectroscopically in the sky fibers.)

As discussed above, the condition `ZWARNING = 0` designates that the BOSS pipeline has determined a confident classification and redshift for a spectrum. The primary source of `ZWARNING  $\neq$  0` spectra is the  $\Delta\chi_r^2$  threshold. However, several other flags are also encoded bit-wise in the `ZWARNING` mask, as documented in Table 3. The definitions of the `ZWARNING` mask-bits in BOSS are identical to their definitions in SDSS-I/II. Two of the bits have been disabled for BOSS DR9, and are only retained for historical consistency: (1) the `NEGATIVE_MODEL` bit, which was previously triggered by stellar model fits with negative amplitudes, which are now disallowed entirely; and (2) the `MANY_OUTLIERS` bit, which was found to flag too many good, high-S/N quasar redshifts in BOSS.

Table 4 summarizes the number of PCA template and polynomial degrees of freedom associated with each spectroscopic object class, along with the name of the file containing the template basis within the `idl1spec2d/v5.4_45` software product. In most cases, the number of PCA templates and number of polynomial terms used in the redshift and classification analysis match the SDSS-I/II `idl1spec2d` values. The one exception is the number of CV star templates, which has decreased from four in SDSS-I/II to three in BOSS due to a smaller available training sample at the time the DR9 code version was frozen. For all target classes we have verified that the choices are nearly optimal by performing tests of the completeness and purity of classification and redshift measurement (relative to visually inspected subsets) as a function of the size of the PCA

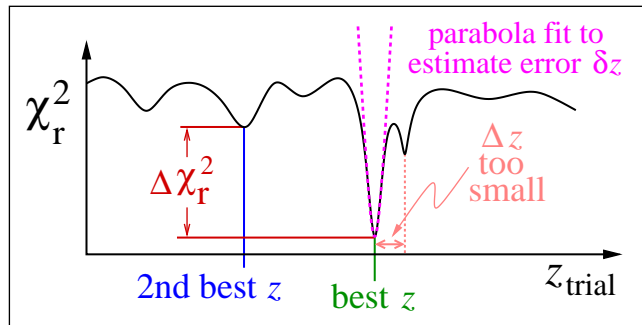


FIG. 2.— Schematic illustration of the `idl1spec2d` redshift measurement algorithm. The reduced  $\chi^2$  curve as a function of redshift (*black curve*) is determined from the best-fit linear combination of template basis spectra at each trial redshift value. The best redshift is defined by the location of the global minimum (*green*). Subsidiary minima separated by less than  $1000 \text{ km s}^{-1}$  are not considered to be separate (*pink*). The curvature of a parabolic fit to the  $\chi_r^2$  curve at the global minimum (*magenta*) is used to determine the best-fit redshift error estimate. The second-best redshift fit is determined by the location of the second-lowest well-separated  $\chi_r^2$  minimum (*blue*). The difference  $\Delta\chi_r^2$  (*red*) between best and second-best redshifts is used to assign confidence in the measurement, as described in the text.

and polynomial basis. As can be expected, increasing the number of PCA and polynomial terms used for the modeling of a particular class increases both the completeness and the *impurity* of the resulting sample for that class. Increases in impurity arise from both catastrophic mis-classification and catastrophic redshift error, with the former decreasing the completeness of other classes. Each spectrum in the survey is fitted with all classes of objects in order to determine a spectroscopic redshift and classification that is independent of photometric data and targeting information (but see §3.2 below).

### 3.2. Special galaxy target handling

The implementation of the `idl1spec2d` redshift code is designed to meet the BOSS scientific requirements on redshift success rates, as discussed in the Introduction. The original SDSS-I/II code operated on spectra alone, without imposing classification or redshift priors based on photometric data or other targeting information. At the S/N typical of SDSS-I/II spectra, this technique proved highly successful, resulting in a redshift success rate better than 99% for the main galaxy sample and a negligible incidence of catastrophic errors. For the BOSS galaxy samples, however, some prior information from the targeting photometric catalog is needed to achieve the required redshift success rate. Specifically, we have found in practice that the LOWZ and CMASS targets can be galaxies, stars, or superpositions of the two, but are almost never quasars (however, see Item 2 in §6.) Without using any prior information, the redshift code produces an excess of erroneous quasar classifications for CMASS targets due to unphysical quasar basis-plus-polynomial combinations yielding the global minimum- $\chi^2$  (see panel “a” in Figure 15 further below.)

To remedy this, the adopted BOSS survey values for the redshifts of LOWZ and CMASS galaxy targets are taken from the parameters `Z_NOQSO` and `CLASS_NOQSO`, together with the associated statistical error estimates `Z_ERR_NOQSO` and confidence flags `ZWARNING_NOQSO`, which represent the best-fit redshift

TABLE 3  
BOSS DR9 REDSHIFT AND CLASSIFICATION WARNING FLAGS (ZWARNING)

Bit	Name	Definition
0	SKY	Sky fiber
1	LITTLE_COVERAGE	Insufficient wavelength coverage
2	SMALL_DELTA_CHI2	$\Delta\chi_r^2$ between best and second-best fit is less than 0.01 (or $0.01 \times$ the minimum $\chi_r^2$ )
3	NEGATIVE_MODEL	Synthetic spectrum negative, <b>disabled for BOSS DR9</b>
4	MANY_OUTLIERS	More than 5% of points above $5\text{-}\sigma$ from synthetic spectrum, <b>disabled for BOSS DR9</b>
5	Z_FITLIMIT	$\chi^2$ minimum for best model is at the edge of the redshift range
6	NEGATIVE_EMISSION	Negative emission in a quasar line at $3\text{-}\sigma$ significance or greater (see §3.3)
7	UNPLUGGED	Broken or unplugged fiber

and classification determined through the procedure described in §3.1, but *excluding the consideration of quasar template fits*. This effectively imposes the red-color and extended-image priors of the galaxy target sample over the blue-color and point-like image priors of the quasar target sample. The SMALL\_DELTA\_CHI2 bit for the ZWARNING\_NOQSO mask is set only on the absolute criterion of  $\Delta\chi_r^2 < 0.01$  relative to the next-best non-quasar model (i.e., with no relative  $\Delta\chi_r^2$  cut). We recommend the use of these “NOQSO” quantities for statistical analyses of the BOSS galaxy samples. The parameter Z and its associated values are also retained and reported for consistency with the original SDSS-I/II approach, representing the global minimum- $\chi^2$  redshift inclusive of all spectral template classes.

### 3.3. Parameter measurements

The primary outputs of the analysis code described in this work are the classification, redshift, redshift error, and best template-based model fit to each spectrum. The code also measures a number of parameters assuming the best-fit classification and redshift. Specifically: stellar velocity dispersions are measured for objects classified as galaxies; emission-line parameters are measured for all objects; and supplemental stellar sub-classifications and radial velocities are measured for objects classified as stars. We now describe these three measurement procedures in turn.

Stellar velocity dispersions  $\sigma_v$  of galaxies are measured using a stellar template basis derived from the ELODIE library (Prugniel & Soubiran 2001), covering the rest-frame spectral range 4100 Å–6800 Å. The high-resolution ELODIE spectra are degraded to the binning scale and approximate resolution of the co-added BOSS spectra, and a PCA of the library is performed. The first 24

TABLE 4  
SUMMARY OF BOSS REDSHIFT & CLASSIFICATION DEGREES OF FREEDOM

Class	Template	$N_{\text{temp}}, N_{\text{poly}}$ Per Fit <sup>1</sup>
	Filename	
GALAXY	spEigenGal-55740.fits	4, 3
QSO	spEigenQSO-55732.fits	4, 3
STAR <sup>2</sup>	spEigenStar-55734.fits	1, 4
STAR (CV)	spEigenCVstar-55734.fits	3, 3

<sup>a</sup> $N_{\text{temp}}$  is number of basis templates per fit;  $N_{\text{poly}}$  is number of additive polynomial background terms used in addition to template basis in the fit.

<sup>b</sup>There are a total of 123 non-CV stellar subtypes considered, but each trial fit only includes a single template.

principal components are used as a basis for fitting the galaxy spectra. The entire PCA basis is incrementally broadened from 0 to  $850 \text{ km s}^{-1}$  in units of  $25 \text{ km s}^{-1}$ , and the set of all broadened PCA components is cached for the analysis of all galaxy spectra. For each galaxy spectrum, the stellar PCA basis is redshifted to match that galaxy’s redshift. At each trial broadening, the galaxy spectrum is fit with an error-weighted least-squares linear combination of the broadened stellar PCA basis plus a quartic polynomial, while masking the regions surrounding common emission lines. This marginalization over stellar-population effects at each trial  $\sigma_v$  value serves to absorb some of the systematic errors of “template mismatch” into the statistical velocity dispersion error. The  $\chi^2$  goodness-of-fit statistic for the best model is tabulated for each broadening step, to define a  $\chi^2(\sigma_v)$  curve. The minimum- $\chi^2$  velocity-dispersion value (with sub-grid localization) is reported as the measured value VDISP, and the error on this measurement VDISP\_ERR is estimated from the curvature of the  $\chi^2$  function at the position of the minimum. Note that this analysis is highly analogous to the redshift measurement procedure described in §3.1. This velocity dispersion measurement algorithm is unchanged from SDSS-I/II.

Within the BOSS data set, the S/N per pixel in galaxy spectra is often below the threshold commonly adopted as minimally sufficient for accurate point estimation of the stellar velocity dispersion. However, it has been shown by Shu et al. (2012) that unbiased measurements of the *distribution* of velocity dispersions within a large sample of galaxies can be made even when the individual spectra are of low S/N, by means of a hierarchical analysis that marginalizes statistically over the likelihoods of all possible velocity-dispersion values for each galaxy. To enable such analyses, we also compute and report the velocity-dispersion likelihood function for each galaxy in the vector-valued column VDISP\_LNL. This is defined by  $-\chi^2(\sigma_v)/2$  for velocity dispersions  $\sigma_v$  from 0 to  $850 \text{ km s}^{-1}$  in steps of  $25 \text{ km s}^{-1}$ . The baseline and overall  $\chi^2$  computation method are the same as described above for the measurement of the VDISP point estimators. However, the VDISP\_LNL calculation employs only the first five stellar PCA template basis spectra, and also marginalizes over galaxy redshift uncertainties. An additional difference is that while the VDISP computations are done only for objects with CLASS of galaxy (for consistency with the SDSS-I/II practice), the VDISP\_LNL calculations are done only for objects with CLASS\_NOQSO of galaxy (for consistency with BOSS practice).

Emission-line parameters for the 31 transitions listed

in Table 5 are computed for all spectra for which those lines fall into the observed BOSS wavelength range. Each line is modeled as a Gaussian, and the amplitudes, centroids, and widths of all lines are optimized non-linearly to obtain a minimum- $\chi^2$  fit to the data. The background continuum spectrum is taken from the best-fit velocity-dispersion model (for galaxies), from the best-fit redshift-pipeline model (for stars), and from a linear fit to the sidebands of each line (for quasars and for ranges of the galaxy spectra that extend beyond the coverage of the ELODIE-based velocity-dispersion templates.) All lines are constrained to have the same redshift within the fit, with the exception of Ly $\alpha$ , which is allowed to fit at a different redshift to account for the asymmetric effects of Ly $\alpha$  forest absorption. In addition, groups of lines are constrained to have the same line-width as noted in Table 5, so as to allow robust fits to the strengths of low-S/N emission lines. Hence, the reported line-widths are effectively a strength-weighted average over the group. An initial guess for the line redshifts is taken from the best-fit pipeline redshift. Emission-line redshifts are allowed to depart arbitrarily from this value, but in practice are well-constrained in cases with significant emission in any lines. 96% of the quasars with significant CIV emission have line fits within  $6000 \text{ km s}^{-1}$  of the template redshift, and 96% of the galaxies with significant [OII] emission have fits within  $100 \text{ km s}^{-1}$ . Line fluxes, line widths, line redshifts, estimated continuum levels, and observed-frame equivalent widths are reported by the line fitting code, along with associated errors. In the SDSS-I/II implementation of the `idlspec2d` emission-line measurement code, equivalent widths were measured relative to the estimated continuum spectrum at line center, while for BOSS DR9 this has been changed to use a continuum level estimated from the sidebands of the line.

Based on the results of the line-fitting code, galaxy spectra with emission in all four of the lines H $\beta$ , [OIII] 5007, H $\alpha$ , and [NII] 6583 detected at 3-sigma or greater are sub-classified into AGN, STARFORMING, and STARBURST according to the following rules. First, galaxies are sub-classified as AGN if

$$\log_{10}([OIII]/H\beta) > 1.2 \log_{10}([NII]/H\alpha) + 0.22 \quad (1)$$

(Baldwin et al. 1981). For galaxies falling on the other side of this cut, sub-classification is made based on the equivalent width of H $\alpha$ : STARFORMING if less than  $50 \text{ \AA}$ , and STARBURST if greater. Galaxies and quasars may be given an additional sub-classification as BROADLINE if they have line widths in excess of  $200 \text{ km s}^{-1}$ , with line-width measurement significance of at least 5-sigma, and line-flux measurement significance of at least 10-sigma.

For spectra classified as stars, an additional fitting to the ELODIE stellar library (Prugniel & Soubiran 2001) is performed. The ELODIE library contains 709 stars spanning spectral types O to M, luminosity classes V to I, and metallicities [Fe/H] from  $-3.0$  to  $+0.8$ . The observed resolution was 42,000 over the wavelength range 4100 to 6800  $\text{\AA}$ . Our fitting makes use of the release of this library at resolution 10,000 that was calibrated to 0.5% in narrow-band spectrophotometric precision and 2.5% in broad-band precision. This library was trimmed from 709 to 610 stars that are not binary or triple stars. The ELODIE spectra are convolved with Gaus-

TABLE 5  
EMISSION LINES MEASURED BY THE BOSS PIPELINE

Line Wavelength <sup>1</sup>	Line Name	Redshift Group <sup>2</sup>	Width Group <sup>3</sup>
1215.67	Ly $\alpha$	Ly $\alpha$	Ly $\alpha$
1240.81	Nv 1240	emission	Nv
1549.48	CIV 1549	emission	emission
1640.42	HeII 1640	emission	emission
1908.734	CIII] 1908	emission	emission
2799.49	MgII 2799	emission	emission
3726.032	[OII] 3725	emission	emission
3728.815	[OII] 3727	emission	emission
3868.76	[NeIII] 3868	emission	emission
3889.049	H $\epsilon$	emission	Balmer
3970.00	[NeIII] 3970	emission	emission
4101.734	H $\delta$	emission	Balmer
4340.464	H $\gamma$	emission	Balmer
4363.209	[OIII] 4363	emission	emission
4685.68	HeII 4685	emission	emission
4861.325	H $\beta$	emission	Balmer
4958.911	[OIII] 4959 <sup>4</sup>	emission	emission
5006.843	[OIII] 5007 <sup>4</sup>	emission	emission
5411.52	HeII 5411	emission	emission
5577.339	[OI] 5577	emission	emission
5754.59	[NII] 5755	emission	emission
5875.68	HeI 5876	emission	emission
6300.304	[OI] 6300	emission	emission
6312.06	[SIII] 6312	emission	emission
6363.776	[OI] 6363	emission	emission
6548.05	[NII] 6548 <sup>5</sup>	emission	emission
6562.801	H $\alpha$	emission	Balmer
6583.45	[NII] 6583 <sup>5</sup>	emission	emission
6716.44	[SII] 6716	emission	emission
6730.82	[SII] 6730	emission	emission
7135.790	[ArIII] 7135	emission	emission

<sup>1</sup>Wavelengths are quoted in air for optical transitions and in vacuum for UV transitions below 2000  $\text{\AA}$ .

<sup>2</sup>Emission lines of a common “redshift group” are constrained to have the same redshift in the line fitting procedure.

<sup>3</sup>Emission lines of a common “width group” are constrained to have the same intrinsic velocity width in the line fitting procedure.

<sup>4</sup>[OIII] 5007 and [OIII] 4959 are constrained to have a 3:1 line-flux ratio.

<sup>5</sup>[NII] 6583 and [NII] 6548 are constrained to have a 3:1 line-flux ratio.

sian functions to match the resolution of the BOSS spectra. A later release of this library (ELODIE 3.1) was not used due to extensive masking of regions near sky emission that compromises its use for measuring radial velocities to high precision (Prugniel et al. 2007). Each BOSS spectrum classified as a star is re-fit to all spectra in this trimmed ELODIE library with the identical redshift-fitting code used to determine the primary redshift (§3.1). These fits are limited to the 4100–6800  $\text{\AA}$  wavelength range, include 3 polynomial terms, and span velocities from  $-1000$  to  $+1000 \text{ km s}^{-1}$ . The physical parameters of the best-fit ELODIE template are included in the pipeline outputs (ELODIE\_TEFF, ELODIE\_LOGG, ELODIE\_FEH), along with the redshift (ELODIE\_Z), statistical error of the redshift (ELODIE\_Z\_ERR) and reduced  $\chi^2$  of that fit (ELODIE\_RCHI2). An estimate of the template-mismatch effects on the redshift is provided as the standard deviation in redshift among the best 12 ELODIE template fits (ELODIE\_Z\_MODELERR).

The BOSS pipeline also computes and reports me-



TABLE 6  
DR9 REDSHIFT AND CLASSIFICATION PIPELINE OUTPUT FILES<sup>1</sup>

<code>spZbest-pppp-mmmmm.fits</code>	Best-fit redshift & class param.s
<code>spZall-pppp-mmmmm.fits</code>	Parameters for all fits
<code>spZLine-pppp-mmmmm.fits</code>	Emission-line parameters
<code>spAll-v5.4.45.fits</code>	Summary param.s for all spectra
<code>spAllLine-v5.4.45.fits</code>	Line fit param.s for all spectra

<sup>a</sup>The strings `pppp` and `mmmm` represent the 4-digit PLATE and 5-digit MJD identifiers for files that are created on a plate-by-plate basis. The string `v5.4.45` denotes the frozen version of the `id1spec2d` software used for the processing of the DR9 spectroscopic data sample. Full documentation of these and other pipeline output files are found at <http://www.sdss3.org/dr9/>

dian spectroscopic signal-to-noise ratios per  $69 \text{ km s}^{-1}$  pixel (`SN_MEDIAN`) over the five SDSS broadband wavelength ranges (*ugriz*, Fukugita et al. 1996), along with the synthetic broadband fluxes predicted by the spectrum (`SPECTROFLUX`) and the best-fit template model to the spectrum (`SPECTROSYNFLUX`).

As described in Ahn et al. (2012), DR9 also includes catalogs of alternative parameter measurements for BOSS galaxies, which are documented in other publications. Chen et al. (2012) describe PCA-based stellar-population parameter measurements and velocity-dispersion estimates. Thomas et al. (2012) have measured stellar velocity dispersions using the pPXF software of Cappellari & Emsellem (2004) and emission-line properties using the GANDALF software of Sarzi et al. (2006). Finally, Maraston et al. (2012) have derived photometric stellar-mass estimates for BOSS galaxies. All these measurements are distributed with DR9, but are separate from the core `id1spec2d` pipeline system described here.

### 3.4. Output files

The BOSS `id1spec2d` redshift pipeline generates output files for each plate, along with summary files to aggregate photometric and spectroscopic parameters across the entire BOSS survey data set. These files are listed in Table 6; together they contain all the parameters described in this paper. Access to these files on the SDSS-III Science Archive Server (SAS), as well as full data-model documentation of their formats and contents, can be obtained through the SDSS-III DR9 website. The `spAll` summary file from the BOSS pipeline is analogous but not identical in form and content to the `specObj` file loaded by the SDSS-III Catalog Archive Server (CAS), which contains both SDSS-I/II and BOSS data.

Approximately 8% of BOSS spectra are repeat observations of previously observed targets, due both to re-observations of entire plates and to re-targeting of a number of objects on more than one plate (see Dawson et al. 2012). Of particular note within the summary files, the best spectroscopic observation of each object (defined by a  $2''$  positional match) in the survey is defined according to the following rules:

1. Prefer spectra with positive median S/N per spectroscopic pixel within the *r*-band wavelength range over other observations.
2. Prefer spectra with `ZWARNING = 0` over other spec-

tra (or `ZWARNING_NOQSO = 0` for galaxy-sample targets.)

3. Prefer spectra with higher median S/N per spectroscopic pixel within the *r*-band wavelength range.

The best observation for each object is designated by setting the parameter `SPECPRIMARY` equal to 1 in the `spAll` file, while setting it equal to zero for all other spectroscopic observations of a given object that may be present within the survey data set.

## 4. TEMPLATE CLASSES

In order to compare and select among galaxy, quasar, and stellar models objectively and with the highest statistical significance, the BOSS pipeline requires redshift and classification measurement templates that span both the full space of physical object types within the survey and the full wavelength range of the spectrograph. BOSS expands on SDSS-I/II in both regards, and hence requires a new set of pipeline templates, which we now describe.

### 4.1. Galaxies

The `id1spec2d` galaxy redshifts for SDSS-I/II were measured using templates generated from 480 galaxies observed on SDSS plate 306, MJD 51690.<sup>24</sup> Redshifts for this training set were established by modeling each spectrum across a range of trial redshifts as a linear combination of (1) the leading two components of a PCA analysis of 10 velocity-standard stars in M67 observed by SDSS-I plate 321 on MJD 51612, (2) a set of common optical emission lines modeled as narrow Gaussian profiles, and (3) a low-order polynomial. The adopted redshift for each galaxy was taken from the location of the minimum- $\chi^2$  value localized to sub-grid accuracy, in the same manner described in §3.1 above. Using these redshifts, the training-sample spectra were transformed to a common rest-frame baseline, and input to an iterative PCA procedure that accounts for measurement errors and missing data (e.g., Tsalmantza & Hogg 2012 and references therein). The leading four “eigenspectra” from this procedure were taken to define the galaxy redshift template basis for SDSS-I/II. For the commissioning analysis of BOSS spectra, these same templates were used for measuring galaxy redshifts, despite their lack of  $z = 0$  coverage redward of  $9300 \text{ \AA}$  and their underrepresentation of post-starburst galaxies (which appear with more frequency in the BOSS CMASS sample than in SDSS-I/II).

To generate a new redshift template set for use in automated analysis of BOSS spectra, we select a set of BOSS galaxies with redshifts over the interval  $0.05 < z < 0.8$  that are well-measured by the original SDSS templates. To increase S/N and flatten the coverage of galaxy parameter space before performing a PCA to generate the template set, we bin together galaxies with similar  $4000 \text{ \AA}$  break strengths (*D*4000, Balogh et al. 1999) and redshifts, for the purposes of stacking their spectra. We use a *D*4000 range from 1.0 to 2.2 with a binning interval of 0.2, and a redshift binning interval of 0.05. In some

<sup>24</sup> These spectra are tabulated in the file `eigeninput_gal.dat` within the `templates` subdirectory of the `id1spec2d` product.

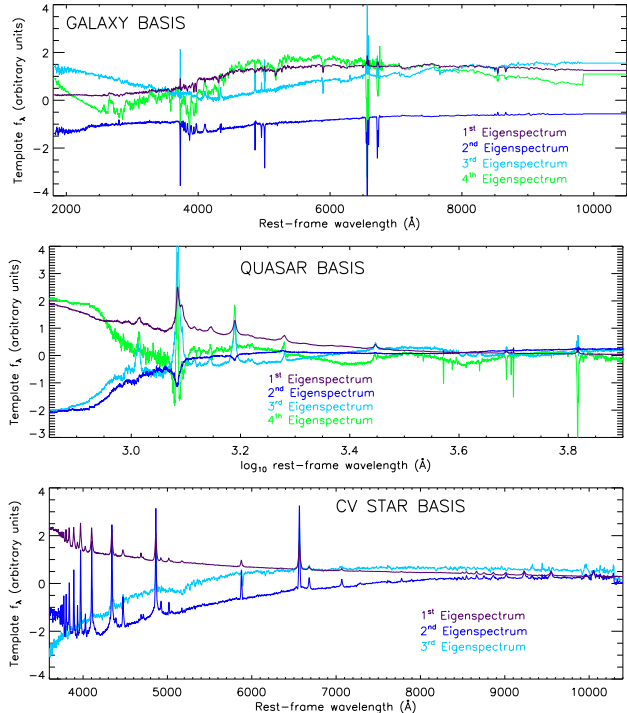


FIG. 3.— BOSS redshift and classification template basis sets for galaxies (*top*), quasars (*middle*), and CV stars (*bottom*).

$D4000$ –redshift bins, we further subdivide the galaxies into several  $H\delta_A$  sub-bins. The number of sub-bins depends on the number of galaxies in each  $D4000$ –redshift bin: if the total number is smaller than 600, we do not divide further into  $H\delta_A$  sub-bins; if the number is in the range 600–1200, we divide into two sub-bins; and if there are greater than 1200, we divide into three sub-bins.

We also select a set of “post-starburst” galaxies from the BOSS galaxy sample, defined by having either

$$D4000 < 1.3 \text{ and } (H\delta_A + H\gamma_A)/2 > 7 \quad (2)$$

or

$$(H\delta_A + H\gamma_A)/2 > \max[-17.50 \times D4000 + 29.25, 3]. \quad (3)$$

This criterion leads to a sample of about 2400 post-starburst galaxies, which we divide into five bins in redshift with equal numbers of galaxies per bin. We then stack the rest-frame spectra of all galaxies in each bin, to generate a set of high-S/N stacked spectra across the range of parameters indicated.

Once all these stacked spectra are in hand, we fit stellar continuum models to them (Brinchmann et al. 2004; Tremonti et al. 2004) using simple stellar population (SSP) models. Our SSP models are taken from Maraston et al. (2009) and Maraston & Strömbäck (2011), and are based on a combination of theoretical and observational stellar library data from Rodríguez-Merino et al. (2005), Sánchez-Blázquez et al. (2006), and Gustafsson et al. (2008). In the rest-frame wavelength range 1900–9900Å, we patch the stacked spectra with the fitted continuum models for pixels with S/N smaller than 10, pixels where the difference between models and stacks is larger than 30%, and pixels where there are no observations. We also add  $H\alpha$ , [NII], and [SII] emission lines for cases where these lines fall out-

side the range of observed wavelengths used to generate the stacked spectra. This is accomplished by selecting galaxies with similar  $D4000$ ,  $H\delta_A$ , and dust extinction as the galaxies used to make the stacks, and computing the median values of  $\sigma_{H\alpha}/\sigma_{H\beta}$ ,  $f_{H\alpha}/f_{H\beta}$ ,  $\sigma_{[NII]}/\sigma_{[OIII]}$ ,  $f_{[NII]}/f_{[OIII]}$ ,  $\sigma_{[SII]}/\sigma_{[OIII]}$ , and  $f_{[SII]}/f_{[OIII]}$  for these comparison samples (here,  $\sigma$  is Gaussian line dispersion and  $f$  is line flux). By multiplying these ratios with the appropriate line width or flux of  $H\beta$  or [OIII] from the stacks, we predict the line widths and fluxes for  $H\alpha$ , [NII] and [SII] to be added to the stacked spectra, which we do using a Gaussian model for each line.

At the end of this process, we have 160 stacked and patched spectra. We augment these data with a sample of 28 type-II quasars (e.g., Zakamska et al. 2003; Reyes et al. 2008) identified within the BOSS spectroscopic data set (see the discussion in §6). This full set of spectra is then used as input to the rest-frame spectrum PCA algorithm to generate the four-component BOSS galaxy redshift template basis, which is shown in the top panel of Figure 3.

#### 4.2. Quasars

Quasar redshift templates are generated from a training sample of targets selected from the SDSS DR5 quasar catalog (Schneider et al. 2007) and targeted for re-observation with the BOSS spectrographs. The targets were chosen from the catalog at random, while enforcing as uniform a distribution as possible in redshift. As of 2011 June 10, 571 objects from this sample had been observed by BOSS. Removal of three spectra for localized cosmetic defects gives a training sample of 568 BOSS quasars. The distribution in redshift of the targeted sample and the observed sample is shown in Figure 4. The observed sample is weighted more heavily above redshift  $z = 2.2$ , in accordance with overlapping BOSS quasar sample priorities. We keep this weighting in the training set, since we want our redshifting performance to be particularly well tuned for the redshift range of interest to the BOSS Ly $\alpha$  forest program.

Using the redshifts given by Schneider et al. (2007), we shift these training spectra to their rest frames and perform a PCA of the sample, with iterative replacement to fill in missing data. The top four principal components are retained and used as the linear basis set for our automated redshift and classification measurements, and are shown in the middle panel of Figure 3.

We do not employ the redshift estimates of Hewett & Wild (2010) for the quasar-template training sample because the current BOSS pipeline is not configured to incorporate the absolute-magnitude information that would be necessary to take advantage of the increased precision afforded by these redshifts. Future BOSS pipeline versions may incorporate the Hewett & Wild (2010) approach. We note that the primary criterion for BOSS spectroscopic pipeline performance on quasar targets is to minimize catastrophic redshift failures. Several detailed approaches to maximizing quasar redshift precision are being investigated within the BOSS quasar science working group, but all of these rely on having essentially correct initial quasar redshifts from the `idl1spec2d` pipeline and/or visual inspection procedures (Pâris et al. 2012).

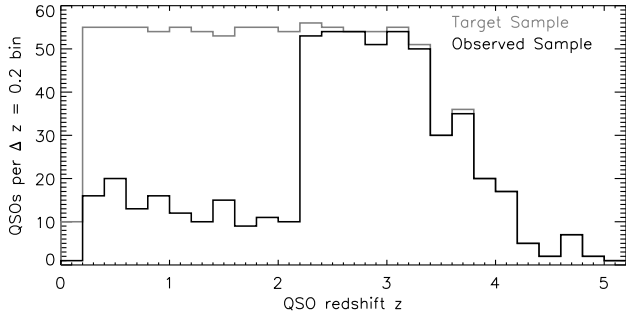


FIG. 4.— Redshift distribution of 1000 targeted (gray) and 571 observed (black) quasar training spectra. Spectra from the observed distribution are used to construct the PCA-based quasar redshift templates used for automated classification and redshift measurement in BOSS DR9 and shown in the middle panel of Figure 3.

### 4.3. Stars

Although stellar science is not a primary goal of BOSS, the redshift pipeline must successfully flag stars from within the galaxy and quasar target samples of the survey. There is currently no comprehensive library of observed stellar spectra covering the full usable wavelength range of the BOSS spectrograph and the full H-R diagram. To assemble a set of stellar templates suitable to BOSS spectrum classification, we use a hybrid approach that extends data from the Indo-US observational stellar spectrum library (Valdes et al. 2004), selected to provide uniform coverage of the space of stellar atmosphere parameters  $T_{\text{eff}}$ ,  $\log g$ , and  $[\text{Fe}/\text{H}]$  using theoretical atmosphere models computed using the MARCS (Gustafsson et al. 2008, for cool stars), ATLAS (Kurucz 2005, for intermediate stars), and CMFGEN (Hillier & Miller 1998, for hot stars) codes, obtained via the curated POLLUX spectrum database (Palacios et al. 2010).

#### 4.3.1. Template spectrum creation

We start with the full database of 1273 Indo-US stellar spectra, which have a resolution of approximately  $1 \text{ \AA}$ , a reduced pixel scale of  $0.4 \text{ \AA}$ , spectral coverage over  $3400 < \lambda < 9500$ , and good flux calibration for most stellar types. The original radial-velocity zeropoints for the library were established either from literature or from velocity-standard cross-correlations. Since classification is the primary function of these spectra within the BOSS pipeline, we do not attempt any further refinement of these velocity zeropoints.

We initialize a “bad pixel” mask for each Indo-US spectrum based upon the zero-value Indo-US pixel mask convention. Furthermore, we define the following telluric absorption bands, and mask all pixels within them:  $6850 \text{ \AA} - 6950 \text{ \AA}$ ,  $7150 \text{ \AA} - 7350 \text{ \AA}$ ,  $7560 \text{ \AA} - 7720 \text{ \AA}$ ,  $8105 \text{ \AA} - 8240 \text{ \AA}$ ,  $> 8900 \text{ \AA}$ . We then select the subset of spectra that meet the conditions of (1) wavelength coverage from at least  $3500 \text{ \AA}$  to  $8900 \text{ \AA}$ , (2) good data over at least 75% of their pixels, (3) flux calibration with a non-flat (i.e., stellar) standard, and (4) no single gap within the spectrum larger than  $200 \text{ \AA}$  (the largest adopted telluric band width). These cuts result in a sample of 879 spectra covering spectral types from O6 to M8, but exclude carbon stars (which are fluxed with a flat SED in the Indo-US

library).

We then take the 1040 model atmosphere spectra from the POLLUX database ranging in temperature from 3000 K to 49000 K, convolved and binned to the resolution and sampling of the Indo-US spectra. For each Indo-US spectrum in our subset, we loop over all model atmospheres and determine the multiplicative scaling of the model that minimizes the sum of squared data-minus-model residuals over non-masked pixels. We adopt the model spectrum that gives the overall minimum sum of squared residuals as being the “best fit” for a particular data spectrum.

The “best fit” model spectrum for each data spectrum is used to extend the data wavelength coverage and interpolate over the data gaps as follows. We define a running window of  $\pm 400$  pixels ( $\pm 160 \text{ \AA}$ ) about an output pixel of interest, and determine the multiplicative scale and tilt to apply to the model over that window in order to give the best (least squares) fit to the non-masked data pixels over that same range. The scaled and tilted model is evaluated at the central pixel to define the new, locally scaled model spectrum, and the process is repeated over the entire spectrum by sliding the window. For pixels centered outside the outermost pixel of data coverage on the red and blue ends, the scale and tilt at the outermost data-covered pixel are used. The data and “sliding-scaled” model spectra are combined into a single output spectrum by assigning 100% model in pixels where the data have no coverage, defining a 100-pixel ( $40 \text{ \AA}$ ) transition region on either side of data gaps where the output spectrum is a weighted combination of the data and the sliding-scaled model, and varying the weight linearly from 0% model + 100% data to 100% model + 0% data over the transition region. Finally, we convolve and bin these output spectra down to the typical resolution (about  $3 \text{ \AA}$  FWHM) and reduced-spectrum sampling ( $\Delta \log_{10} \lambda = 0.0001$  per pixel) of the BOSS data, also transforming from air to vacuum wavelengths to match the BOSS spectrum convention.

#### 4.3.2. Archetype subset selection

From these 879 patched and extended stellar spectra, our goal is to select a representative subset of “archetypes” that provide sufficient coverage of stellar parameter space to perform automated spectroscopic star-galaxy and star-quasar separation, while not attempting overly detailed stellar analysis that is beyond the scope of the BOSS science mission (cf. Lee et al. 2008).

We first visually inspect the template database and remove a single spectrum with noticeable data quality issues in an unmasked data region (Indo-US ID#33111,  $5450 \text{ \AA} < \lambda < 6000 \text{ \AA}$ ). We also select the 12 template spectra that have significant emission lines, and retain each of them for our final archetype set. This leaves 866 spectra from which to select the remainder of our archetype sample.

To select a subset of archetypes from the remaining set of templates, we wish to make use of a measure of the degree of similarity or difference between any two spectra. We first restrict our attention to the wavelength range  $3400 \text{ \AA} - 11000 \text{ \AA}$ , corresponding to  $N_{\text{pix}} = 5099$  pixels at the processed  $69 \text{ km s}^{-1}$  BOSS spectrum pixel scale. We

then re-normalize all the template spectra to satisfy

$$\sum_{i=1}^{N_{\text{pix}}} f_i^2 = N_{\text{pix}} , \quad (4)$$

where  $f_i$  is the flux density (in the  $f_\lambda$  sense) in pixel  $i$ . We define a statistic  $s^2$  measuring the quality of spectrum  $f'$ , scaled by a factor  $a$ , as a model for spectrum  $f$ :

$$s^2 = \sum_{i=1}^{N_{\text{pix}}} (f_i - a f'_i)^2 . \quad (5)$$

With our normalization convention, the best-fit (minimum- $s^2$ ) scaling is simply given by

$$a_{\text{best}} = N_{\text{pix}}^{-1} \sum_{i=1}^{N_{\text{pix}}} f_i f'_i , \quad (6)$$

and the value of  $s^2$  at this best scaling is given by

$$s_{\text{best}}^2 = N_{\text{pix}}(1 - a_{\text{best}}^2) . \quad (7)$$

Note that  $a_{\text{best}}$  and  $s_{\text{best}}^2$  are symmetric under the interchange of  $f$  and  $f'$ : the amplitude and fit quality of one template to another does not depend upon which one is taken as the “data” and which one as the “model”. Thus  $s_{\text{best}}^2$  can be regarded as a measure of how different two templates are from one another.

We compute the matrix of  $s_{\text{best}}^2$  between all pairs of templates in our set, and determine our archetype list in an iterative procedure. We set a threshold of 7.5 for the maximum  $s_{\text{best}}^2$  allowable between two spectra in order for one spectrum to be an acceptable representative for the other. This threshold was selected heuristically to tune the size and diversity of the final sample. We then identify the single template spectrum within the sample that has the most  $s_{\text{best}}^2 < 7.5$  matches to the rest of the sample. This spectrum and all the spectra that it matches are removed from further consideration, and the process is iterated until all spectra have been accounted for in this manner. For our chosen threshold, this process identifies 105 archetypes out of 866 analyzed templates. When added to the 12 emission-line templates, this yields a set of 117 stellar templates for our automated spectrum classification algorithm. Spectra fit by these templates are tagged with the stellar subclass listed in the Indo-US database, along with the library identification number of the archetype spectrum.

#### 4.3.3. Special stellar subclasses

Several subclasses of star appear with some frequency in the BOSS target sample, but are not represented in the (flux-calibrated) Indo-US library. For these subclasses, representative training samples from within the BOSS data set are identified based upon classification using SDSS-I/II stellar templates. New templates are derived by averaging the spectra of these training sets within a PCA framework. The six subclasses and the number of training spectra for each of them are: (1) 47 carbon stars; (2) 50 “hotter” white dwarfs with  $u - g < 0.3$ ; (3) 50 “cooler” white dwarfs with  $u - g \geq 0.3$ ; (4) 19 calcium white dwarfs; (5) 31 magnetic white dwarfs; and (6) 50

L dwarfs. In addition, a sample of 18 cataclysmic variable stars (CVs) with prominent emission lines is used to define a CV star eigenbasis of 3 PCA modes, which is shown in the bottom panel of Figure 3. Because of the use of multiple eigenvectors rather than a single average spectrum, CV stars are treated as an object class separate from other stars in the automated classification analysis.

## 5. PERFORMANCE AND VERIFICATION

Table 1 provides a summary of the BOSS DR9 spectroscopic data set analyzed by the redshift and classification pipeline described in this work, along with a number of summary performance statistics that we now examine. Additional checks on the `idlSpec2d` pipeline performance for galaxy targets in comparison with the `zcode` cross-correlation redshift software described by Cannon et al. (2006) are presented in Dawson et al. (2012), and additional discussion of pipeline quasar classification and redshift performance is found in Pâris et al. (2012). The BOSS DR9 sample contains 831,000 spectra. Of these, about 0.2% are lost to unplugged fibers and spectra falling along bad CCD columns. Approximately 92% of the BOSS DR9 spectra are of unique objects (as defined by a 2'' positional match). The remaining 8% are repeat spectra from overlapping plates or repeat observations of the same plate.

### 5.1. Galaxy redshift completeness and purity

Using the `Z_NOQSO` redshift measurement convention as described in §3.2, we achieve an automated completeness (i.e., `ZWARNING_NOQSO == 0` rate) of 98.7% for the CMASS sample and 99.9% for the LOWZ sample (from Table 1). Restricting further to objects that are spectroscopically classified as galaxies (`CLASS_NOQSO == "GALAXY"`), we find combined targeting and measurement completeness percentages of 95.4% for CMASS and 99.2% for LOWZ. These percentages satisfy the BOSS science requirement of at least 94% overall galaxy redshift success. For the CMASS sample, about 70% of the (small) survey inefficiency is due to targeting stars and star-galaxy superpositions rather than galaxies, and about 30% arises from known redshift measurement failures.

To verify the completeness and quantify the purity of the automated galaxy redshifting and classification, we make use of a “truth table” generated by the first author from the visual inspection of 4864 galaxy spectra taken on eight plates observed during 2010 March.<sup>25</sup> We focus primarily on the CMASS sample, as this higher-redshift (and thus lower S/N) sample poses the greatest challenge to the software. Of the inspected spectra, 3666 are CMASS targets that are above the fiber-magnitude threshold, not unplugged, and not falling on bad CCD columns. From among these 3666 galaxy-sample spectra, 3627 have confidently measured pipeline redshifts and classifications, giving an automated completeness of 98.9%, consistent with the completeness of the full DR9 CMASS sample from above. Of this subset, 3500 are classified as galaxies (as opposed to stars) by the pipeline, giving a 95.5% overall sample completeness including

<sup>25</sup> The plates are: 3804 of MJD 55267; 3686, 3853, and 3855 of MJD 55268; and 3687, 3805, 3856, and 3860 of MJD 55269.

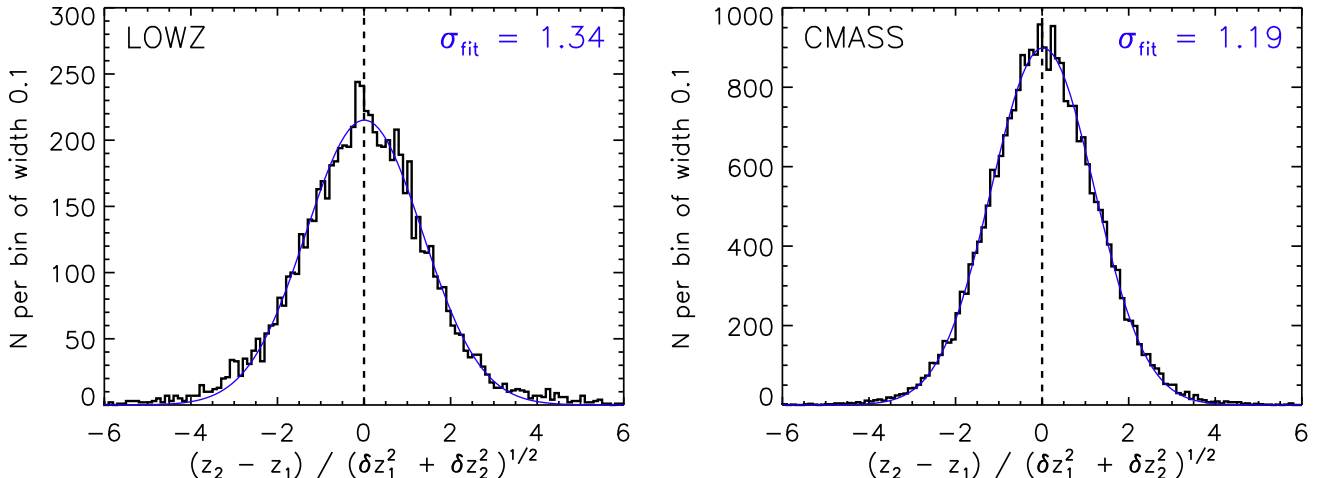


FIG. 5.— Histograms of redshift differences of LOWZ (left) and CMASS (right) galaxies that are observed more than once, scaled by the quadrature sum of statistical error estimates in each epoch. Over-plotted are the best-fit Gaussian models, with a dispersion parameter of  $\sigma = 1.34$  for the LOWZ sample and  $\sigma = 1.19$  for the CMASS sample.

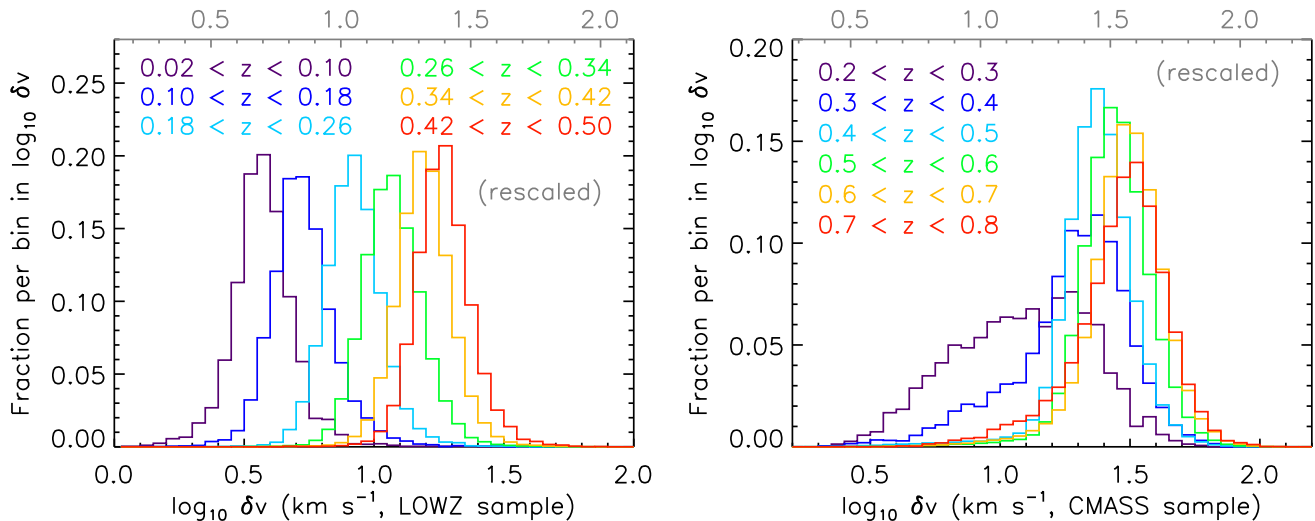


FIG. 6.— Distribution of estimated *statistical* galaxy redshift errors for LOWZ (left) and CMASS (right) sample galaxies over multiple redshift ranges. The horizontal axes at bottom indicate raw error estimates; the gray horizontal axes at top indicate errors rescaled by the factors illustrated in Figure 5.

target-selection efficiency, which is also consistent with the sample-wide value.

To quantify the purity of the CMASS spectroscopic redshift sample, we first search for “catastrophic” impurities in the CMASS redshift sample, defined as spectra for which the pipeline reports a confident galaxy classification and redshift, but for which the visual inspection yields a confident classification (of any class) with a redshift that differs by greater than  $\Delta z = 0.005$ . This search yields three such spectra out of 3500: two are definite galaxy–M-star superpositions, and the other is a possible galaxy–galaxy superposition (for which the pipeline redshift is more convincing in retrospect than the inspection redshift). We next check for less clearly defined impurities, defined as spectra for which the pipeline reports a confident galaxy classification and redshift, but for which the visual inspection does not yield a confident result. This search identifies 10 such spectra, six of which are plausible pipeline redshifts with subjective

visual judgments of low S/N, and the remaining four of which are due to artifacts associated with spectrum combination across the spectrograph dichroic at  $6000 \text{ \AA}$  (see Item 3 in §6). Taking the three superposition spectra and the four artifact spectra as genuine contaminants, we find a CMASS sample impurity rate of about 0.2%, satisfying the 1% maximum catastrophic redshift failure rate specified as the scientific requirement for BOSS.

To check for the possibility of recoverable incompleteness, we examine CMASS spectra for which the visual inspections yield a confident galaxy classification and redshift, but for which the automated pipeline yields either no confident result (i.e., `ZWARNING_NOQSO` > 0), or a classification as a star. There are 26 such spectra, which break down as follows: 11 low-S/N spectra for which the pipeline’s lack of confidence is statistically defensible; 5 definite or possible galaxy–galaxy superpositions; 4 definite or possible star–galaxy superpositions; 3 spectra with artifacts; 2 broadline AGN mistaken for stars

(but with correct quasar-class redshifts that are excluded by the Z\_NOQSO convention); and 1 narrow-line AGN for which the pipeline confuses [OIII] 5007 and H $\alpha$ . Taking the 11 noisy but visually convincing redshifts and the three AGN spectra to represent the recoverable sample, we find an excess incompleteness of about 0.4% relative to the maximum attainable given the data.

To further assess the effects of star–galaxy superpositions (for which the pipeline takes no special approach), we search a set of 57910 CMASS spectra from 150 plates for instances of a best-fit non-quasar class of GALAXY and a next-best non-quasar class of STAR, and examine these spectra visually for the presence of significant stellar features. From this sample, we find 103 possible and 58 probable star–galaxy superpositions, indicating a total CMASS star–galaxy superposition rate of between 0.1% and 0.2%. These star–galaxy superpositions that are given a spectroscopic class of GALAXY are a source of sample impurity, as the galaxies are typically neither bright enough nor of the correct color to fall within the CMASS color–magnitude selection cuts on their own. Any star–galaxy superpositions classified as STAR by the pipeline are excluded from the large-scale structure analysis and contribute only to target-selection inefficiency.

Our visual inspection set also contains 568 LOWZ galaxies brighter than the fiber-magnitude threshold. All of these spectra are confidently classified and redshifted by both the pipeline and the visual inspection, with three classified as stars. This is consistent with the automated completeness and stellar contamination rate for the full LOWZ sample, with no detectable incidence of catastrophic failures.

### 5.2. Galaxy redshift precision

Redshift errors are calculated from the curvature of the  $\chi^2$  function in the vicinity of the minimum value that is used to determine the best-fit redshift measurement. To assess the accuracy of these statistical error estimates, we make use of a set of 27170 repeat observations of CMASS targets and 7503 repeat observations of LOWZ targets within the DR9 data set. We reference all repeat observations to the SPECPRIARY observation of a given object, and scale the redshift difference between the two observations by the quadrature sum of the error estimates from the two epochs. We then construct a histogram of these scaled velocity differences and fit it with a Gaussian function. If the estimated errors accounted for all the statistical uncertainty, these fitted Gaussians would have a dispersion parameter of unity. Figure 5 shows the results of this analysis, with fitted dispersions of  $\sigma = 1.34$  for the LOWZ sample and  $\sigma = 1.19$  for the CMASS sample. Thus, while slightly underestimated, the redshift errors are impressively close to being statistically accurate. The greater scatter (relative to the statistical error estimates) for the LOWZ sample suggests that systematic effects become more important at higher S/N.

This analysis of repeat spectra also yields 44 CMASS re-observations that have absolute redshift differences  $|\Delta z| > 0.005$  between the two epochs. These are primarily due to galaxy–galaxy superpositions at distinct redshifts, un-masked spectrum artifacts, and a number of type II quasars for which broad [OIII] 5007 emission is confused with H $\alpha$  in one epoch but not the other (see

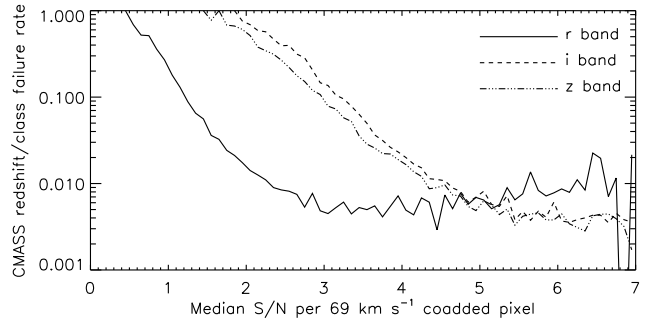


FIG. 7.— BOSS CMASS sample redshift and classification failure rate (i.e., ZWARNING\_NOQSO > 0) as a function of median spectroscopic S/N within the SDSS  $r$  (solid),  $i$  (dashed), and  $z$  (dot-dashed) bandpass regions of the spectrum.

Item 2 in §6). The implied 0.16% CMASS redshift impurity rate is consistent with the value found from the truth-table tests of §5.1. For the LOWZ repeat observations, two spectra yield  $|\Delta z| > 0.005$ , both of which are galaxy–galaxy superpositions.

For all CMASS and LOWZ targets, we also compute the distribution of estimated redshift errors as a function of redshift. These distributions are shown in Figure 6. In all cases, typical errors are a few tens of  $\text{km s}^{-1}$  even when scaled up to reflect the super-statistical scatter displayed in Figure 5. These errors are well below the  $300 \text{ km s}^{-1}$  redshift precision requirement of the BOSS galaxy large-scale structure science analyses.

### 5.3. Galaxy redshift success dependence

As in any redshift survey, spectroscopic S/N is the primary determinant of redshift success in BOSS. Figure 7 shows the dependence of the CMASS galaxy redshift failure rate as a function of the median spectroscopic signal-to-noise ratio over the SDSS  $r$ ,  $i$ , and  $z$  bandpass ranges, which represent the most relevant regions of the spectrum for measuring continuum redshifts of passive galaxies over the redshift interval  $z \approx 0.4$ – $0.8$ . Failure is defined in the sense of ZWARNING\_NOQSO > 0, so that targets confidently identified as stars are counted as a success for the pipeline even though they represent a failure in the larger sense of galaxy targeting and redshift measurement. We see a decrease in the failure rate as a function of  $r$ -band S/N up to  $S/N_r \simeq 3$ , where an asymptotic minimum of  $\approx 5 \times 10^{-3}$  is reached. For CMASS spectra with  $S/N_r = 3$ , the typical value for both  $S/N_i$  and  $S/N_z$  is approximately 6, consistent with the S/N values in those bands at which the asymptotic failure rate is reached in Figure 7.

Galaxy magnitude correlates strongly with spectroscopic S/N and hence with redshift success: this is the motivation for the formal CMASS sample limit of  $i$ -band magnitude brighter than 21.5 within a  $2''$ -diameter BOSS fiber. To gauge the dependence of redshift completeness on this limit, Figure 8 shows the CMASS sample redshift failure rate as a function of  $i_{\text{fiber}}$ , selecting the best single observation of each target. Targets fainter than  $i_{\text{fiber}} = 21.5$  are available from a more permissive CMASS cut applied during commissioning observations. At the formal CMASS cutoff, the marginal failure rate is about 7%.

The characteristics of the BOSS spectrograph optics and CCD detectors produce a weak dependence of red-

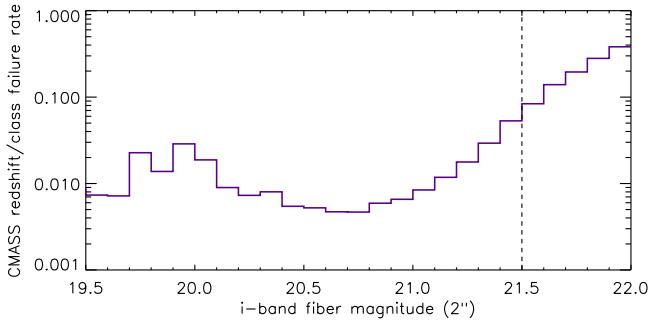


FIG. 8.— CMASS sample failure rate as a function of apparent (not extinction-corrected)  $i$ -band magnitude within the  $2''$ -diameter BOSS fiber, using the best single spectroscopic observation of each CMASS target in the DR9 data set. Vertical dashed line at 21.5 indicates the nominal fiber-magnitude faint limit of the CMASS sample.

shift success rate on fiber identification number along the linear spectrograph slit-heads. Figure 9 presents this dependence for the CMASS sample. This figure is generated only for targets brighter than the  $i_{\text{fiber}} < 21.5$  cut, but includes all survey spectra of each target (i.e., no SPECPRIMARY cut) so as to give an unbiased picture of performance versus fiber number. The upturns near fiber numbers 1, 500, and 1000 are associated with the edges of the spectrograph camera fields of view, and are described further in Item 4 in §6 below. The effects of isolated bad CCD columns are also evident, and are described in Item 5 in §6. The failure rate is slightly higher on average for fibers above 500, corresponding to a lower end-to-end survey-averaged throughput for the optics and CCDs of spectrograph 2 as compared to those of spectrograph 1.

In principle, variations in the quality of sky foreground subtraction can also affect spectroscopic redshift success. In practice, we do not see this effect in BOSS. Figure 10 shows the spectrum of systematic sky-subtraction residual flux measured from the sky-subtracted blank-sky fibers of a representative BOSS plate, calculated by subtracting statistical spectrum pixel estimates in quadrature from the root-mean-square (RMS) residual spectrum across all sky fibers on the plate. At the positions of bright OH air-glow lines, the systematic residuals are generally at or below 1% of the sky flux. To test whether the redshift failure rate is affected significantly by variations in sky-subtraction quality, we quantify the level of residual flux from the sky-subtraction process in

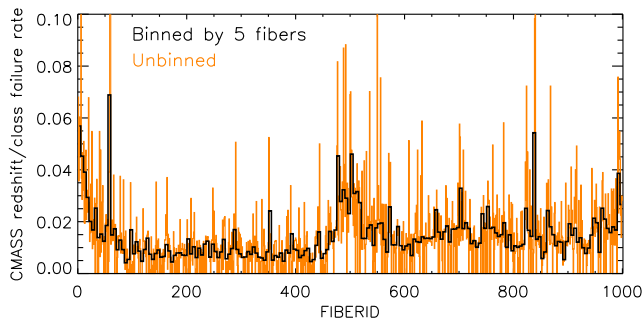


FIG. 9.— CMASS sample failure rate as a function of fiber number. Generated for all spectroscopic observations of CMASS sample targets with  $i_{\text{fiber}} < 21.5$ . Large-scale structure is due to spectrograph camera optics, and small-scale peaks are associated with bad CCD columns.

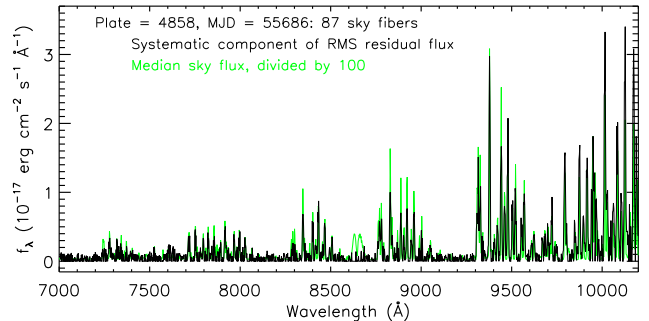


FIG. 10.— Systematic sky-subtraction RMS residual spectra (black line) computed from sky-subtracted blank sky fibers of a representative BOSS plate. Estimated statistical errors have been subtracted in quadrature from RMS residual flux at each wavelength. Also shown is the median sky flux spectrum scaled down by a factor of 100.

each plate as the RMS flux in all sky-subtracted blank-sky fibers over the wavelength range  $8300\text{\AA}$  to  $10400\text{\AA}$ , where the effects of OH air-glow lines are particularly pronounced. Figure 11 displays the results of this test, with RMS residual flux expressed both in units of estimated statistical significance and in units of specific flux. In both cases, there is no discernible correlation between sky-subtraction residual scale and redshift failure rate. The two conclusions we draw are that (1) the quality of BOSS sky subtraction is uniformly high, and (2) residual variations in the quality of this sky subtraction do not significantly affect redshift measurement for the passive, continuum-dominated CMASS galaxies.

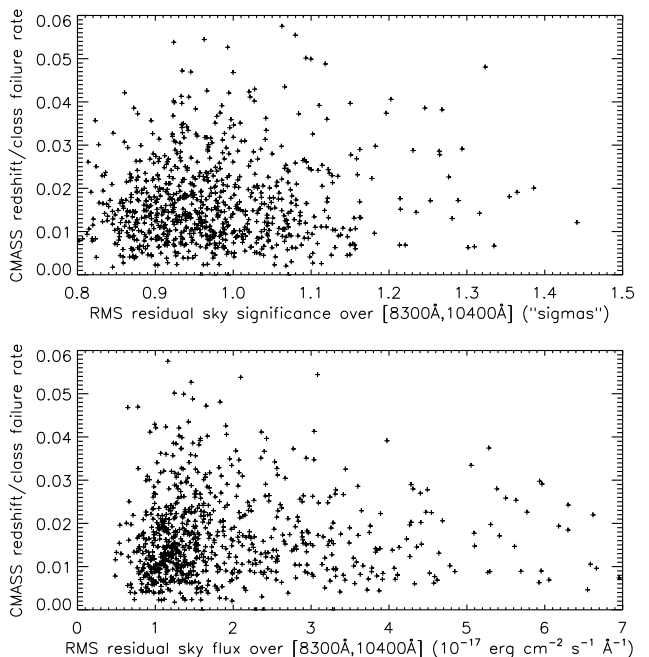


FIG. 11.— CMASS sample redshift and classification failure rate versus RMS residual flux in sky-subtracted sky fibers, for BOSS plates with at least 300 CMASS galaxy sample targets. Each point represents one PLATE-MJD. The top panel abscissa is in units of statistical significance, while the bottom panel is in units of specific flux. No correlation is seen. RMS significance values of less than “1-sigma” reflect unaccounted pixel-to-pixel correlations introduced by the re-binning and co-addition of spectra.

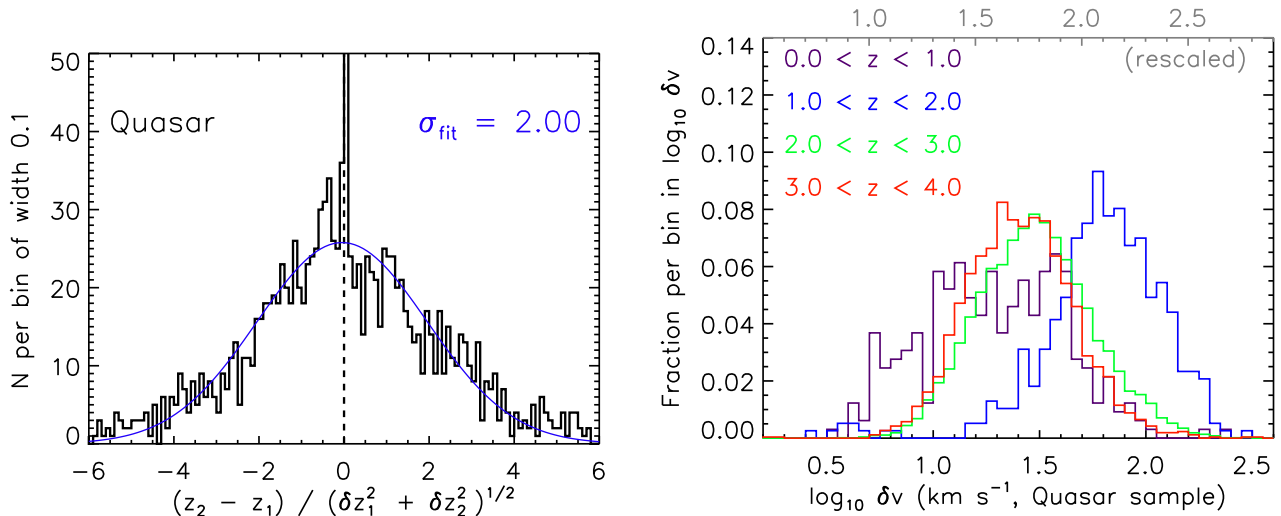


FIG. 12.— Distribution of error-scaled redshift differences between repeat observations of BOSS quasars (*left*), and distribution of estimated single-epoch *statistical* quasar redshift errors for multiple redshift ranges (*right*). True quasar redshift errors are likely dominated by systematic effects not reflected here. The upper and lower horizontal axes in the right-hand plot are as in Figure 6.

#### 5.4. Quasar redshift success

Unlike the BOSS galaxy samples, the BOSS quasar sample does not have a stated requirement on automated classification and redshift success. The entire quasar target sample is being manually inspected to provide a catalog of visually verified classifications and redshifts (Pâris et al. 2012), for which the automated BOSS pipeline redshifts provide the initial default value. From Table 1, we find that the `id1spec2d` pipeline reports a confident classification and redshift (i.e., `ZWARNING == 0`) for about 79% of the unique spectra of the BOSS quasar target sample. The majority of the remaining 21% of the quasar sample observations are low-S/N spectra of faint targets. Approximately 51.5% of the unique observed quasar sample targets are spectroscopically confirmed as quasars; most of the confidently classified non-quasar spectra are stars (typically of spectral type F) occupying the same region of color space as quasars in the targeted redshift range. However, only 33.6% of the unique target sample are confirmed quasars at the redshifts  $2.2 < z < 3.5$  which are the focus of the BOSS Ly $\alpha$  forest analysis (Dawson et al. 2012). Figure 13 presents the spectroscopic confirmation rate for quasars in this redshift range  $2.2 < z < 3.5$ , as a function of median S/N per pixel over the  $g$ -band wavelength range.

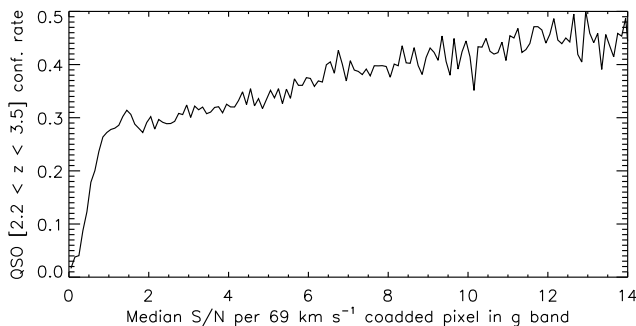


FIG. 13.— Spectroscopic confirmation rate of quasars with redshift  $2.2 < z < 3.5$  from among BOSS quasar sample targets, as a function of median  $g$ -band S/N per spectroscopic pixel.

The full comparison of visual redshifts and pipeline redshifts for BOSS quasar-sample targets is presented in Pâris et al. (2012), and is beyond the scope of this current work. We note two particular statistics here. First, the visual inspections provide a 1.7% increase in the sample of  $2.2 < z < 3.5$  quasars beyond those that are confidently identified by the automated pipeline. Second, 0.6% of the quasars identified confidently by the pipeline at  $2.2 < z < 3.5$  either have redshifts in disagreement by  $|\Delta z| > 0.05$  with the visual-inspection values, or do not have confident visual identification despite having been inspected. The latter are due mostly to extremely broad absorption-line quasars and to line mis-identifications. The overall conclusion, however, is that the completeness and purity of the automated quasar classification and redshift measurement is quite high.

Figure 12 shows the distribution of error-scaled redshift differences for 1464 repeat BOSS observations of confirmed quasars, as well as the redshift-dependent distributions of statistical single-epoch redshift error estimates, analogous to Figures 5 and 6 for galaxies. For quasars, the *statistical* pipeline redshift errors are underestimated by a factor of approximately two, although the true errors in the pipeline quasar redshifts are likely dominated by systematic effects. Eight of the repeat observations, or about 0.5%, give a redshift difference of  $|\Delta z| > 0.05$ , consistent with the rate of catastrophic errors found by the comparison with the visual inspections. The redshift range 1.0–2.0 is particularly difficult since the observed optical spectra do not have either the narrow [OIII] 5007 line or the strong Ly $\alpha$  line to guide the template fit.

#### 5.5. Stellar radial velocity precision

We now briefly examine the precision and accuracy of BOSS stellar radial velocities based on stellar repeat observations. Specifically, we identify 8174 repeat observations of objects classified as `STAR` with `ZWARNING == 0` for both epochs. In Figure 14, we plot the velocity difference between the two epochs of these repeats against the quadrature sum of their statistical error estimates. We



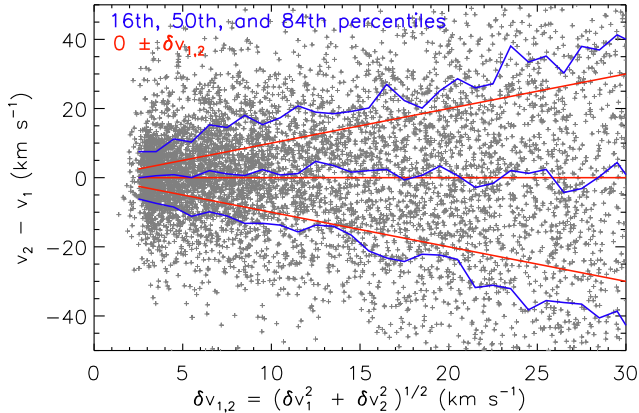


FIG. 14.— Velocity difference between epochs for 8174 stars with more than one good spectrum in the BOSS data set, as a function of the quadrature sum of statistical error estimates from the two differenced epochs. Also plotted are the 16<sup>th</sup>, 50<sup>th</sup>, and 84<sup>th</sup> percentile curves of this velocity difference (blue) and the expected statistical  $0 \pm 1\sigma$  lines (red).

see that the distribution becomes tighter at higher S/N as expected, with reasonably good agreement between estimated statistical error and actual velocity differences above approximately  $15 \text{ km s}^{-1}$  in combined statistical error (or approximately  $10 \text{ km s}^{-1}$  in single-epoch error). Subtracting the statistical error estimates in quadrature from the half-difference between the 84<sup>th</sup> and 16<sup>th</sup> percentile velocity differences, and dividing by a factor of  $\sqrt{2}$  to convert to a single-epoch value, we find a systematic radial-velocity floor of approximately  $4.5 \text{ km s}^{-1}$  at the high S/N end, comparable to the  $4 \text{ km s}^{-1}$  precision attained for bright stars by the SEGUE project in SDSS-I/II (Yanny et al. 2009).

## 6. KNOWN ISSUES

In order to freeze a set of reductions for collaboration analysis and public release, we have accepted the presence of a number of known outstanding issues in the software that either were deemed small enough in a statistical sense within the survey, or were discovered after the software freeze deadline. These issues are documented in the following list, and several are illustrated in Figure 15.

1. PCA fits of the GALAXY and QSO classes can sometimes yield unphysical basis combinations at low S/N. This effect is part of the motivation for the Z\_NOQSO redshifts described in §3.2, and is illustrated in panel “a” of Figure 15. In order to enable a targeting-blind spectroscopic classification of the sort used in SDSS-I/II, this effect could be remedied by priors on physical PCA coefficient combinations, or by non-negativity requirements on archetype-based models such as are used for non-CV stellar classifications in `id1spec2d`. These alternatives are the subject of ongoing development for future BOSS data releases.
2. A small number of type II quasars (e.g., Zakamska et al. 2003) at redshift  $z \sim 0.5$  are selected by the CMASS cuts due to their colors, but their obscured-AGN spectra are not typical of the majority of galaxies used to train the galaxy

redshift templates. The inclusion of several such systems in the galaxy-template training set has addressed this issue partially, but a number of these objects have a best-fit galaxy-template redshift that confuses broad [OIII] 5007 for H $\alpha$ . Their quasar-template redshifts are generally correct, but due to the Z\_NOQSO redshift strategy employed for the BOSS galaxy samples (§3.2), their adopted redshifts are often in error (see panel “b” of Figure 15.) Since these objects represent such a small percentage of the BOSS galaxy target samples, these errors were deemed acceptable for DR9 galaxy-clustering analyses.

The fundamental problem is that the spectra of type II quasars are sufficiently different from the spectra of most BOSS galaxies that we cannot span the space of both categories with the current number of PCA templates (four) in the single GALAXY basis set. In future BOSS data releases, we anticipate addressing this issue through either higher-dimensional basis sets with physical coefficient priors, sub-division of the GALAXY class into several subclasses each with its own basis set, or an archetype-based galaxy redshifting algorithm.

3. A small number of spectra are affected by cross-talk from bright stars (generally spectrophotometric standards) in neighboring fibers. This is often manifested in a strong break feature at the dichroic transition around  $6000 \text{ \AA}$  (see panel “c” of Figure 15), due to different levels of cross-talk between the red and blue arms of the spectrograph (Smee et al. 2012). These effects appear to occur less frequently at later survey dates, presumably because of improvements in the operating focus of the BOSS spectrographs. We intend to address these effects in future BOSS data releases through improvements in the extraction codes, and to flag any spectra that remain compromised. No masking of this effect is implemented for BOSS DR9 data, however, except to the extent that it sometimes triggers a ZWARNING flag.
4. As discussed in §5.3 and shown in Figure 9, the BOSS redshift success rates are somewhat dependent on fiber number in the sense that fibers near the edge of the spectrograph camera fields of view (FIBERID values near 1, 500, and 1000) have lower success rates. Longer-term development of new extraction codes based on the 2D PSF-modeling approach of Bolton & Schlegel (2010) is ongoing, and may mitigate this problem to a significant extent.
5. A few columns in the BOSS CCDs are bad only in a transient sense, and are not included in the bad-column masks applied to the CCD frames. These columns lead to occasional spectrum artifacts concentrated near particular fiber numbers (see panel “d” of Figure 15) that are not masked or flagged.
6. White-dwarf, L-dwarf, carbon-star, and cataclysmic-variable star subclasses have less accurate template radial-velocity zero-points in comparison to the stellar archetypes derived from

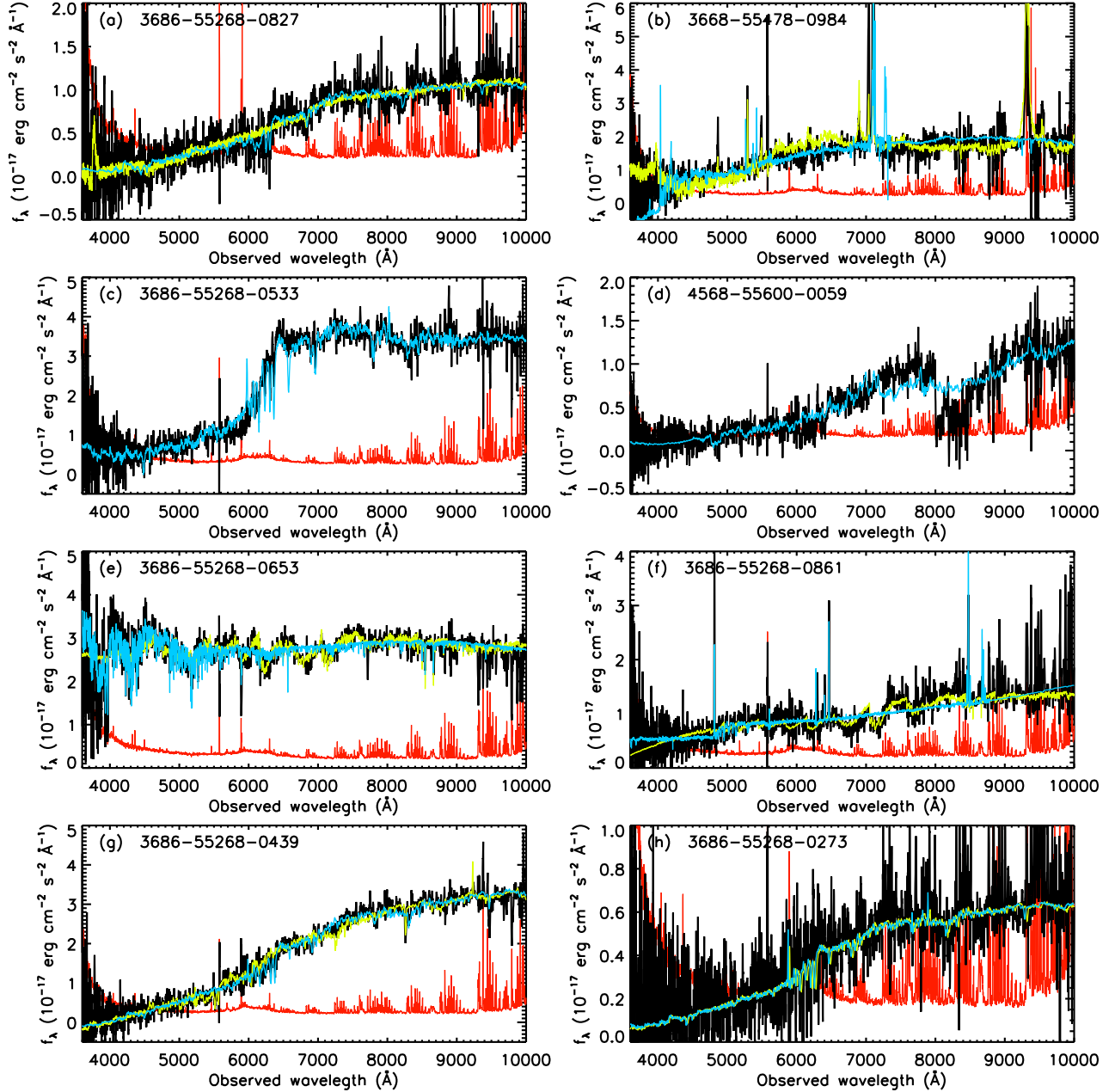


FIG. 15.— Mosaic of problematic BOSS spectra. Black lines show data (smoothed over a 5-pixel window), and red lines show  $1\text{-}\sigma$  noise level estimated by the extraction pipeline. Spectra are labeled by PLATE-MJD-FIBERID. All spectra are from the CMASS sample. Individual objects are: (a) redshift  $z = 0.589$  galaxy for which the overall minimum- $\chi^2$  fit is an unphysical quasar-class model (yellow), but for which the NOQSO redshift and class (cyan) are confident and correct, as described in §3.2; (b) type-II quasar with a correct quasar-class redshift of  $z = 0.419$  (yellow) but an incorrect NOQSO redshift  $z = 0.083$  (cyan) due to confusion of broad [OIII] 5007 with  $H\alpha$ ; (c) spectrum with an exaggerated break feature at the 6000 Å dichroic transition, due to cross-talk effects from a bright star in a neighboring fiber, but for which the pipeline redshift of  $z = 0.603$  (cyan) is nevertheless correct; (d) Spectrum affected by a transient bad CCD column in the region  $8000 \text{ \AA} < \lambda < 9000 \text{ \AA}$ , with an unphysical galaxy-class model (cyan) for which the SMALL\_DELTA\_CHI2 bit is set in the ZWARNING\_NOQSO mask; (e) spectral superposition of a G star with an M star (the spectrum is confidently classified as STAR), with the best-fit G-star-plus-polynomial shown in cyan and the best-fit M-star-plus-polynomial shown in yellow; (f) spectral superposition between a redshift  $z = 0.291$  emission-line galaxy (cyan) and a redshift  $z = 0.402$  absorption-line galaxy (yellow); (g) spectral superposition between a redshift  $z = 0.606$  absorption-line galaxy (cyan) and a redshift  $z = 0.576$  emission-line galaxy (yellow); (h) spectrum of a galaxy for which the pipeline cannot distinguish with statistical confidence between a redshift of  $z = 0.576$  (cyan) and  $z = 0.582$  (yellow, largely hidden by cyan), and for which the SMALL\_DELTA\_CHI2 bit is consequently set in the ZWARNING\_NOQSO mask (see §3.1 and §3.2) since these two redshifts differ by more than  $1000 \text{ km s}^{-1}$ .

the Indo-U.S. library. This issue may be rectified in future data releases, although the primary role of stellar templates in BOSS will remain to correctly classify and set aside non-galaxies and non-quasars.

7. Spectra showing superpositions of two objects are not systematically identified and flagged by the pipeline. While the majority of BOSS spectra are of single objects, superpositions are occasionally found to occur. In some cases, the inclusion of the polynomial terms in the redshift model fitting leads to fits of almost equal quality for the two components individually, leading to a `SMALL_DELTA_CHI2` flag in the `ZWARNING` (or `ZWARNING_NOQSO`) mask. In other cases, one component is dominant and is identified by the pipeline as the confident classification and redshift, but with the second component typically identified by one of the lower-quality fits reported in the `spZa11` file. Various examples of superposition spectra are displayed in Figure 15, including star–star (panel “e”), star–galaxy (panel “f”), and galaxy–galaxy (panel “g”). A systematic search for superposition spectra in the BOSS data set by the BOSS Emission-Line Lens Survey (BELLS, Brownstein et al. 2012) has discovered a large sample of strong gravitational lens galaxies.

## 7. SUMMARY AND CONCLUSION

We have described the “1D” component of the `idlpec2d` pipeline that provides automated redshift measurement and classification for the SDSS-III BOSS DR9 data set, which comprises 831,000 optical spectra. This software is substantially similar to the `idlpec2d` redshift analysis code used for SDSS-I/II data, but has been upgraded with new templates and several new algorithms for application to the BOSS project, and has been presented in great detail for the first time in this work. The pipeline also provides additional parameter measurements, including emission-line fits for all objects, and velocity-dispersion likelihood curves for objects classified as galaxies. The redshift success rate of the `idlpec2d` pipeline is well in excess of the scientific requirements of the BOSS project. The software

provides first-principles estimates of statistical redshift errors that are Gaussian distributed and accurate to within small correction factors. The “2D” component of the `idlpec2d` pipeline that extracts spectra from raw CCD pixels is the subject of Schlegel et al. (2012). Full data-model information for both the 2D and 1D BOSS pipeline outputs can be found at the SDSS-III DR9 website (<http://www.sdss3.org/dr9/>).

Development work continues on data-reduction software for BOSS, both in the calibration and extraction of spectra, and in the classification and redshift analysis procedures. Subsequent BOSS data releases will be accompanied by similar documentation of the implemented results of this ongoing development.

Funding for SDSS-III has been provided by the Alfred P. Sloan Foundation, the Participating Institutions, the National Science Foundation, and the U.S. Department of Energy Office of Science. The SDSS-III web site is <http://www.sdss3.org/>.

SDSS-III is managed by the Astrophysical Research Consortium for the Participating Institutions of the SDSS-III Collaboration including the University of Arizona, the Brazilian Participation Group, Brookhaven National Laboratory, University of Cambridge, Carnegie Mellon University, University of Florida, the French Participation Group, the German Participation Group, Harvard University, the Instituto de Astrofísica de Canarias, the Michigan State/Notre Dame/JINA Participation Group, Johns Hopkins University, Lawrence Berkeley National Laboratory, Max Planck Institute for Astrophysics, Max Planck Institute for Extraterrestrial Physics, New Mexico State University, New York University, Ohio State University, Pennsylvania State University, University of Portsmouth, Princeton University, the Spanish Participation Group, University of Tokyo, The University of Utah, Vanderbilt University, University of Virginia, University of Washington, and Yale University.

This research has made use of the POLLUX database (<http://pollux.graal.univ-montp2.fr>) operated at LUPM (Université Montpellier II - CNRS, France) with the support of the PNPS and INSU.

## REFERENCES

- Adelman-McCarthy, J. K., et al. 2006, *ApJS*, 162, 38  
Ahn, C. P., et al. 2012, *ApJS*, submitted (arXiv:1207.7137)  
Aihara, H., et al. 2011, *ApJS*, 193, 29  
Anderson, L., et al. 2012, *MNRAS*, in press (arXiv:1203.6594)  
Baldwin, J. A., Phillips, M. M., & Terlevich, R. 1981, *PASP*, 93, 5  
Balogh, M. L., Morris, S. L., Yee, H. K. C., Carlberg, R. G., & Ellingson, E. 1999, *ApJ*, 527, 54  
Becker, R. H., White, R. L., & Helfand, D. J. 1995, *ApJ*, 450, 559  
Bolton, A. S., & Schlegel, D. J. 2010, *PASP*, 122, 248  
Bovy, J., et al. 2011, *ApJ*, 729, 141  
Brinchmann, J., Charlot, S., White, S. D. M., Tremonti, C., Kauffmann, G., Heckman, T., & Brinkmann, J. 2004, *MNRAS*, 351, 1151  
Brownstein, J. R., et al. 2012, *ApJ*, 744, 41  
Cannon, R., et al. 2006, *MNRAS*, 372, 425  
Cappellari, M., & Emsellem, E. 2004, *PASP*, 116, 138  
Chen, Y.-M., et al. 2012, *MNRAS*, 421, 314  
Dawson, K. S., et al. 2012, *AJ*, submitted (arXiv:1208.0022)  
Eisenstein, D. J., et al. 2005, *ApJ*, 633, 560  
—. 2011, *AJ*, 142, 72  
Fukugita, M., Ichikawa, T., Gunn, J. E., Doi, M., Shimasaku, K., & Schneider, D. P. 1996, *AJ*, 111, 1748  
Glazebrook, K., Offer, A. R., & Deeley, K. 1998, *ApJ*, 492, 98  
Gunn, J. E., et al. 1998, *AJ*, 116, 3040  
—. 2006, *AJ*, 131, 2332  
Gustafsson, B., Edvardsson, B., Eriksson, K., Jørgensen, U. G., Nordlund, Å., & Plez, B. 2008, *A&A*, 486, 951  
Hewett, P. C., Irwin, M. J., Bunclark, P., Bridgeland, M. T., Kibblewhite, E. J., He, X. T., & Smith, M. G. 1985, *MNRAS*, 213, 971  
Hewett, P. C., & Wild, V. 2010, *MNRAS*, 405, 2302  
Hillier, D. J., & Miller, D. L. 1998, *ApJ*, 496, 407  
Horne, K. 1986, *PASP*, 98, 609  
Kirkpatrick, J. A., et al. 2011, *ApJ*, 743, 125  
Kurucz, R. L. 2005, *Memorie della Società Astronomica Italiana Supplement*, v.8, p.14 (2005), 8, 14  
Lee, Y. S., et al. 2008, *AJ*, 136, 2022  
Manera, M., et al. 2012, *MNRAS*, submitted (arXiv:1203.6609)  
Maraston, C., Nieves Colmenáez, L., Bender, R., & Thomas, D. 2009, *A&A*, 493, 425  
Maraston, C., & Strömbäck, G. 2011, *MNRAS*, 418, 2785

- Maraston, C., et al. 2012, MNRAS, submitted (arXiv:1207.6114)
- Nuza, S. E., et al. 2012, MNRAS, submitted (arXiv:1202.6057)
- Padmanabhan, N., et al. 2012, in preparation
- Palacios, A., Gebran, M., Josselin, E., Martins, F., Plez, B., Belmas, M., & Lèbre, A. 2010, A&A, 516, A13
- Pâris, I., et al. 2012, in preparation
- Prugniel, P., & Soubiran, C. 2001, A&A, 369, 1048
- Prugniel, P., Soubiran, C., Koleva, M., & Le Borgne, D. 2007, arXiv:astro-ph/0703658
- Reid, B. A., et al. 2012, MNRAS, submitted (arXiv:1203.6641)
- Reyes, R., et al. 2008, AJ, 136, 2373
- Rodríguez-Merino, L. H., Chavez, M., Bertone, E., & Buzzoni, A. 2005, ApJ, 626, 411
- Ross, A. J., et al. 2012a, MNRAS, 424, 564
- Ross, N. P., et al. 2012b, ApJS, 199, 3
- Sanchez, A. G., et al. 2012, MNRAS, in press (arXiv:1203.6616)
- Sánchez-Blázquez, P., et al. 2006, MNRAS, 371, 703
- Sandín, C., Becker, T., Roth, M. M., Gerssen, J., Monreal-Ibero, A., Böhm, P., & Weilbacher, P. 2010, A&A, 515, A35
- Sarzi, M., et al. 2006, MNRAS, 366, 1151
- Schlegel, D. J., Finkbeiner, D. P., & Davis, M. 1998, ApJ, 500, 525
- Schlegel, D. J., et al. 2012, in preparation
- Schneider, D. P., et al. 2007, AJ, 134, 102
- Shu, Y., et al. 2012, AJ, 143, 90
- Smee, S., et al. 2012, AJ, submitted (arXiv:1208.2233)
- SubbaRao, M., Frieman, J., Bernardi, M., Loveday, J., Nichol, B., Castander, F., & Meiksin, A. 2002, in Society of Photo-Optical Instrumentation Engineers (SPIE) Conference Series, Vol. 4847, Society of Photo-Optical Instrumentation Engineers (SPIE) Conference Series, ed. J.-L. Starck & F. D. Murtagh, 452–460
- Thomas, D., et al. 2012, MNRAS, submitted (arXiv:1207.6115)
- Tojeiro, R., et al. 2012, MNRAS, submitted (arXiv:1203.6565)
- Tremonti, C. A., et al. 2004, ApJ, 613, 898
- Tsalmantza, P., & Hogg, D. W. 2012, ApJ, 753, 122
- Valdes, F., Gupta, R., Rose, J. A., Singh, H. P., & Bell, D. J. 2004, ApJS, 152, 251
- Yanny, B., et al. 2009, AJ, 137, 4377
- York, D. G., et al. 2000, AJ, 120, 1579
- Zakamska, N. L., et al. 2003, AJ, 126, 2125